



Contents lists available at ScienceDirect

Lithos

journal homepage: www.elsevier.com/locate/lithos

Research Article

Peridotite versus pyroxenite input in Mongolian Mesozoic-Cenozoic lavas, and dykes

 Thomas C. Sheldrick^a, Gregor Hahn^a, Mihai N. Ducea^{b,c,*}, Adriana M. Stoica^b, Kurt Constenius^{c,d}, Matt Heizler^e
^a School of Geography, Geology and the Environment, University of Leicester, University Road, Leicester LE1 7RH, UK^b Faculty of Geology and Geophysics, University of Bucharest, 010041 Bucharest, Romania^c University of Arizona, Tucson, AZ 85721, USA^d Petro Mataad Group, Ulaanbaatar 14240, Mongolia^e New Mexico Bureau of Geology, Socorro, NM 87801, USA

ARTICLE INFO

Article history:

Received 14 May 2020

Received in revised form 13 August 2020

Accepted 14 August 2020

Available online 20 August 2020

Keywords:

Piecemeal delamination

Thermobarometry modelling

Slab graveyard

Mantle upwelling

Argalant range

Mongolia

ABSTRACT

Here we test for peridotite versus pyroxenite input in Mongolian Mesozoic and Cenozoic magmatism. A combination of new ⁴⁰Ar/³⁹Ar radiometric dating results, whole-rock major- and trace-element, Sr–Nd isotope, and mineral phenocryst geochemical data is used to decipher the petrogenesis of Cretaceous lavas (Tsagaan Nuur and Khukh Tolgoi) and dykes (Samaan Damba) from the Argalant Range, Gobi-Altai (Mongolia). This magmatism is compared to Cretaceous asthenospheric mantle-derived basalts from Tsost Magmatic Field and Cenozoic volcanism from the Gobi-Altai, Khangai Range Watershed, Tariat and Togo to assess changing source conditions. We also compare this magmatism to Cenozoic magmatism from the North China Craton. The Argalant Range magmatism has geochemical signatures consistent with the involvement of both peridotite and pyroxenite-like components, and we suggest that this pyroxenite-like component was obtained through the melting of metasomatized subcontinental lithospheric mantle (SCLM). Mineral-liquid thermobarometer results for samples from Khukh Tolgoi and Samaan Damba indicate that upwelling magma stalled at ~30 km depth, before finally traversing further to surface. A model to explain Mesozoic magmatic genesis is presented here, whereby piecemeal delamination and convective erosion of a metasomatized SCLM drives magmatism. The Cenozoic volcanism also has geochemical signatures consistent with the melting of non-peridotite components, and the presence of samples with >9 wt% MgO from Khangai Range Watershed, Tariat and Togo enabled assessments on the relative contribution of non-peridotite melt input. We suggest that magmatism from Togo contains the greatest amount of non-peridotite melt input, followed by Tariat and Khangai Range Watershed localities. We hypothesize that intermittent Cenozoic magmatism is the result of a slab graveyard under East Asia foundering into the upper mantle.

© 2020 Elsevier B.V. All rights reserved.

1. Introduction

Mesozoic and Cenozoic volcanism is abundant in central and eastern Mongolia (Barry et al., 2003; Dash et al., 2015; Enkhbold et al., 2020; Hunt et al., 2012; Käufel et al., 2020; Sheldrick et al., 2020a; Yarmolyuk et al., 2015), NE Russia (Sheldrick et al., 2020b; Vorontsov et al., 2016) and the North China Craton (e.g., Gao et al., 2004; Liu et al., 2019; Menzies et al., 2007; Wu et al., 2019; Zhang et al., 2002) and occurs largely within a Neoproterozoic to Mesozoic orogen known as the Central Asian Orogenic Belt (CAOB), far away from continental margins (e.g., Windley et al., 2007; Xiao et al., 2015). Central Mongolia and NE China is part of the CAOB, and has undergone a complex tectonic

history, affected by the closure of the Paleo-Asian and Mongol-Okhotsk Ocean, and the Paleo-Pacific tectonic regime. However, the nearest ancient subduction zone to much of the Mongolian Mesozoic and Cenozoic volcanic fields was that associated with the closure of the Mongol-Okhotsk Ocean, evident today from the Mongol-Okhotsk suture (Fig. 1), which stretches from central Mongolia in the west, to the Sea of Okhotsk in the east (e.g., Tomurtogoo et al., 2005; Van der Voo et al., 2015). The Mongol-Okhotsk Ocean closed with double-sided subduction (Bussien et al., 2011; Sheldrick et al., 2020a; Windley et al., 2010), from west to east, in a scissor-like fashion (Kravchinsky et al., 2002; Van der Voo et al., 2015), with the final suturing occurring sometime around the Middle Jurassic (Sorokin et al., 2020). Thus, although the closure of the Mongol-Okhotsk Ocean may have metasomatized the subcontinental lithospheric mantle (SCLM) and controlled the dispersal of upwelling mantle, the Late Mesozoic and Cenozoic magmatism itself occurred in an intraplate setting.

* Corresponding author at: Faculty of Geology and Geophysics, University of Bucharest, 010041 Bucharest, Romania.

E-mail address: ducea@email.arizona.edu (M.N. Ducea).

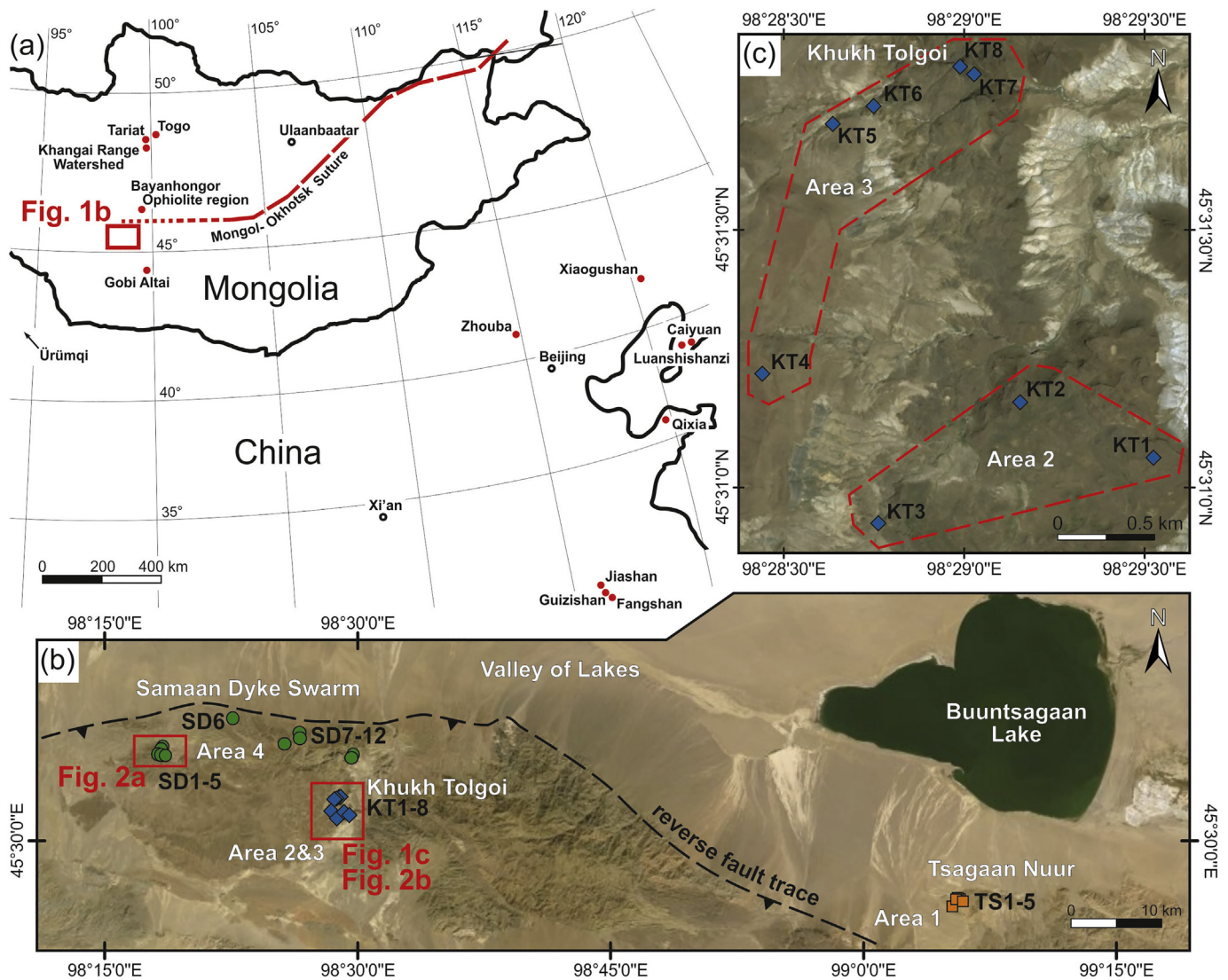


Fig. 1. a) Simplified sketch map of Mongolia showing sample area (boxed area) and the Cenozoic magmatism sample localities from North China included in this study for comparative purposes (Liu et al., 2008). b) Satellite image illustrating the three main sample areas (Digital Globe, 2019). c) Satellite image of Khukh Tolgoi sample area (Digital Globe, 2019).

The North China Craton (NCC) and southern Mongolia underwent widespread removal of lithospheric mantle in the Mesozoic (e.g., Gao et al., 2008; Menzies et al., 2007; Sheldrick et al., 2020b) and associated volcanism is spatially and temporally related to the widespread formation of sedimentary basins (e.g., Johnson et al., 2003; Meng, 2003). Nevertheless, the Mongolian basins have relatively small-scale (half-)grabens that would have accommodated no more than a few kilometers of extension (e.g., Johnson, 2015; Van Hinsbergen et al., 2015) thus making extensional processes alone likely insufficient to cause the magmatism. To help understand what triggered such widespread intraplate magmatism, it is necessary to understand the relationship between magma source composition and melting behavior.

Melting of mantle sources with multiple lithologies, each with its own melting behavior and chemical composition, is an important factor in producing a range of magma compositions (e.g., Hofmann and White, 1982; Lambart et al., 2016). Increasingly, the role of mafic lithologies, such as pyroxenite/hornblendite as a source rock, or as an additional melting component (e.g., as veins in a source rock), has been recognized in magma genesis (e.g., Herzberg, 2006; Pang et al., 2019). Many studies have been done on magmatic rocks globally to try and differentiate between peridotite and pyroxenite source components. These studies have utilized a variety of geochemical techniques, including modelling

on major-element ratios (Yang and Zhou, 2013; Yang et al., 2019), novel isotope studies (Gleeson et al., 2020; Zhang et al., 2019) and interpretation of olivine phenocryst compositions (Herzberg et al., 2014; Sobolev et al., 2007).

High-pressure melting experiments on pyroxene-rich lithologies demonstrate that at a given pressure, pyroxenites have lower solidus temperatures than peridotites (e.g., Petermann and Hofmann and White, 1982; Lambart et al., 2009). Such pyroxenites entrained in an adiabatically upwelling mantle consisting of mostly peridotite would contribute a greater fraction of liquid to the aggregated mantle partial melt than would be inferred from their relatively low mass fraction in the region undergoing melting (Lambart et al., 2016; Stolper and Asimow, 2007). Therefore, could a pyroxenite source component, with a potentially lower solidus temperature than peridotite, have facilitated widespread intraplate magmatism in Mongolia?

This study aims to assess the role of different source components in Mesozoic-Cenozoic lavas and dykes from Mongolia. Here, we analyse a suite of Cretaceous basaltic lavas and dykes from the Argalant Range, Altai-Gobi region of western-central Mongolia (Fig. 1). New whole-rock, Sr–Nd isotope, and mineral phenocryst geochemical data is used to assess source characteristics. We also compare our data to Cenozoic volcanism from the Gobi-Altai, and central Mongolia (Khangai

Range Watershed, Tariat and Togo), and to Cenozoic magmatism from the NCC (Liu et al., 2008), to better understand changes in melting behavior and source composition with time.

Understanding what triggered the magmatism in Mongolia is likely to be key to understanding magmatic processes across East Asia, and in fully understanding the destruction of the NCC.

2. Regional geology

The Argalant Range is part of the Gobi-Altai orogenic zone in central Asia, which forms part of the CAOB (Comeau et al., 2020; Rippington et al., 2013; Windley et al., 2007; Xiao et al., 2015). Tectonic inversion starting in the late Oligocene led to the development of this modern mountain range which has a large active reverse fault bounding it to the north (Cunningham, 2005). The Argalant Range and surrounding areas are comprised of Late Palaeozoic and Triassic basement and contain continental Mesozoic rift sequences (Badarch et al., 2002; Burianek et al., 2012).

The rift sequences consist of sandstone, siltstone, marl and shales, and are interlayered with basalt lavas. Much of the inferred rift structure was inverted in the Cenozoic causing the normal faults to be reactivated as high-angle reverse faults (Burianek et al., 2008; Cunningham, 2005; Johnson et al., 2015). North of the Argalant Range, in the Valley of the Lakes (Fig. 1b), Lower Cretaceous rocks of the Hunteeg Formation (post-rift sequence) and a veneer of Cenozoic deposits unconformably overlie a thick assemblage of pre-rift strata of probable Middle to Late Jurassic age.

The basaltic lavas are interlayered with lacustrine and lacustrine-deltaic sandstones and shales and are cross-cut by dykes. However, despite the development of a half-graben, the Argalant Range lacks typical structures associated with significant extension, such as numerous normal faults and significant *syn*-tectonic deposition and tilting (Johnson et al., 2015). Only three K–Ar dates on Mesozoic trachyandesite and trachybasalt rocks from the Khara-Argalant and Dund-Argalant Range exist in the literature (Yarmolyuk et al., 2015 and references therein), which have an age range between 117 and 113 ± 4 Ma.

3. Sampling strategy & field observations

We collected 25 basaltic samples (Supplementary Material A) from around four main localities (Fig. 1–2) in the Argalant Range: (1) Tsagaan Nuur (south of Buuntsagaan Nuur); (2–3) Khukh Tolgoi; and (4) Samaan Damba dyke swarm and surrounding area.

The Tsagaan Nuur locality is a broad, low relief, anticline where we collected five samples from four distinct lavas (Fig. 1b, 3a), from different stratigraphic positions.

The Khukh Tolgoi sample localities are only separated by a few kilometers. The transects are in two clearly identifiable canyons (Fig. 2a) where basaltic samples at different stratigraphic intervals were collected ($n = 8$). These two canyons are herein separated as Area 2 and Area 3 (Fig. 2a). Area 2 has a broad exposure of lavas, but individual flow boundaries are often unclear (Fig. 3a). Most samples were collected from Area 3 because of good exposure (Fig. 3b–c). Six individual flows reached thicknesses of up to ~40 m and make up the volcanic stratigraphy of the area. Very little sedimentation occurs between the different lavas, indicating that these consecutive lava flows occurred within a short time span. Some of these lava flows continue for >20 km, and the top of the lavas commonly exhibit eroded pahoehoe and a'a surfaces. Columnar jointing is a common feature among the basalt in Area 3 (Fig. 3d–e). Occasional pillow structures were identified indicative of a sub-aqueous/lake environment consistent with the development of the Early Cretaceous sedimentary lacustrine deposits.

The Samaan Damba dyke swarm (Fig. 2b) is in the westernmost part of the Argalant Range that we sampled as Area 4. It occurs after a large area (~600 km²) covered by abundant basalt sheets. Some of the lava flows are visible but most basaltic exposures occur as dykes or small

stocks (Fig. 3f–g) and 12 samples were collected. This impressive dyke swarm has individual dykes ranging from 5 to 30 m wide. Some of these dykes have perperitic textures, which might be from soft sediment interaction in a shallow subaqueous environment. These aphanitic dykes commonly show cross-cutting relationships and columnar jointing. Samples SD10–11 were basaltic clasts collected from within a megabreccia.

4. Petrography

Basaltic samples in the field have brown reddish weathered surfaces, and sometimes exhibit chlorite and serpentine alteration. The freshest samples were selected to minimise the amount of altered material. However, samples still have some phenocryst and groundmass alteration. The lavas (Tsagaan Nuur and Khukh Tolgoi localities) and dykes (Samaan Damba locality) are aphanitic and porphyritic (Fig. 4a–d), and the lavas contain amygdaloids of carbonate material.

The lavas have a fine crystallized groundmass containing phenocrysts of olivine (<1 mm), clinopyroxene (<1 mm) and microphenocrysts of ilmenite and magnetite. Plagioclase feldspar phenocrysts are larger (1–3 mm, occasionally up to 1 cm). Olivine is commonly altered (or partially altered) to iddingsite and there is some alteration of clinopyroxene. Oxides appear as individual crystals, or as alteration products on pyroxene, and as dendritic overgrowths on plagioclase crystals (Fig. 4f). Ophitic clinopyroxene encloses plagioclase crystals and poikilitic plagioclase laths contain magnetite and ilmenite inclusions (Fig. 4a–d). Sample KT4 (Khukh Tolgoi, Area 2) contains an orthopyroxene phenocryst which might be a xenocryst.

The dykes have a crystallized groundmass containing anhedral and euhedral phenocrysts of plagioclase which enclose microphenocrysts of olivine and clinopyroxene. Olivine is commonly altered partially to iddingsite and chlorite. Oxides appear as individual crystals or as dendritic overgrowths on plagioclase crystals (Fig. 4f).

5. Argon dating results

New ⁴⁰Ar/³⁹Ar radiometric dating was performed on groundmass concentrate samples TS3 (Tsagaan Nuur), KT4 (Khukh Tolgoi) and SD1 (Samaan Damba). The ⁴⁰Ar/³⁹Ar age spectra are presented in Fig. 5 and the analytical methods are reported in the online supplementary material.

The samples yield variably complex age spectra with discordance observed in the initial heating steps. Each sample is assigned a plateau age that is interpreted to record the age of the sample. Sample TS3 reveals a climbing age pattern from about 60 Ma to 109 Ma over the first ~20% of ³⁹Ar released followed by a plateau segment consisting of 9 steps. This relatively flat segment incorporates 82.1% of the ³⁹Ar and has a weighted mean age of 109.0 ± 0.2 Ma. Sample SD1 also displays initially young apparent ages before rising to a plateau consisting of 8 steps, incorporating 83.4% of the ³⁹Ar, and a plateau age of 110.4 ± 0.1 Ma. The rising segment of these spectra likely records partial argon loss. Sample KT4 records downward stepping ages over the initial 40% of the spectrum before yielding overall concordant ages for the final 60% of gas release. For sample KT4 a weighted mean age of 112.6 ± 0.1 Ma is calculated from a plateau consisting of 5 steps, which comprises 62.4% of the ³⁹Ar released. The initially old steps of the spectrum likely reveal excess ⁴⁰Ar, however data clustering (constant ⁴⁰Ar radiogenic values) preclude useful isochron analysis. We note that the plateau ages are associated with high MSWD values due to the coupling of minor age variation with very precise error estimates obtained by the multi-collector mass spectrometer on highly radiogenic gas. We do not believe that these high MSWD values preclude accurate age assignment. Thus, the basaltic volcanism in the Argalant Range looks to have been emplaced over ~3 Ma period (109–112 Ma).

6. Geochemical results of the Argalant range magmatic samples

The major-element, trace-element and Sr–Nd isotope analysis, and mineral electron microprobe methodology is reported in the online supplementary material. All analysed data is also available in the online supplementary material.

6.1. Major-element variations

The lava samples from Tsagaan Nuur and Khukh Tolgoi have loss-on-ignition (LOI) values between 1.6 and 5.6 wt%, apart from sample TS1 (13.1 wt%) and TS4 (7.4 wt%). Samples TS1 and TS4 are now omitted from further study. The Samaan Damba dyke swarm (and proximal areas) have LOI values between 0.4 and 4.7 wt%, apart from sample SD4 (7.9 wt%) which is now omitted from further study. We include LOI versus major-element plots in the online supplementary material. However, excluding the omitted samples, sample localities do not show significant correlations between LOI values and major-element compositions – although samples from Khukh Tolgoi show a slight loss in MgO with increasing LOI values.

To classify our samples, we use a total alkali vs. silica (TAS) diagram (Fig. 6a). The Tsagaan Nuur and Khukh Tolgoi lavas plot as basalt to basaltic trachyandesite in composition. The Samaan Damba dykes and surrounding sample localities plot as basalt to trachyandesite in composition, apart from samples SD10 and SD12 which are a trachydacite. Samples typically plot in the within-plate array on the Zr versus Zr/Y discrimination diagram (Fig. 6b), consistent with the magmatism happening in an intraplate setting. On a normative Ne–Ol–Di–Hy–Qz (CIPW) diagram (Fig. 6c) the Tsagaan Nur and Khukh Tolgoi samples plot in the Ol–Di–Hy–Qz fields, below the 1 atm cotectic from Thompson et al. (2001). The Samaan Damba area samples plot in the nepheline–normative to quartz–normative fields, as they become increasingly evolved (i.e. <MgO wt%), and plot below the 1 atm cotectic.

Samples are variably evolved, with Mg-numbers ranging from 38 to 47 for Tsagaan Nuur samples, 46 to 54 for Khukh Tolgoi samples and 20 to 58 for the Samaan Damba samples (Fig. 7).

6.2. Trace-element and REE variations

Chromium and Ni contents correlate positively with Mg-number for Khukh Tolgoi and the Samaan Damba samples (Fig. 7f–g), while there are too few samples from Tsagaan Nuur to confirm such a trend.

Primitive mantle-normalized diagrams (Fig. 8) show that all samples are enriched in the light rare earth elements (LREE) compared to normal mid-ocean ridge basalt (N-MORB) compositions and have elevated LREE relative to heavy rare earth elements (HREE). Samples are also enriched in the high-field strength elements (HFSE) and the large-ion lithophile elements (LILE) compared with N-MORB. The samples show prominent negative Nb, Ta and Ti anomalies, a feature commonly observed in island-arc volcanics, along with the enrichment of fluid-mobile incompatible trace elements (e.g., Ba and K). However, unlike volcanic arc lavas, the samples are enriched in incompatible trace elements like Zr. However, sample TS5 shows many similarities to average continental arc basalt (Fig. 8a: CAB) and has a comparatively low Zr concentration (62 ppm) compared to our other samples.

Unlike Late Cretaceous basalts from the Gobi–Altai (Yarmolyuk et al., 2015), eastern Mongolia (Dash et al., 2015; Sheldrick et al., 2020a) and the North China Craton (Liu et al., 2008; Sheldrick et al., 2020b), our samples have prominent negative Nb and Ta anomalies (Nb/La & Ta/La ≤ 1) and are less depleted in the HREE's compared to Cenozoic basalts from the Gobi–Altai (Fig. 8). Cenozoic basalts from East Asia lack the relative depletion in some HFSEs (Nb, Ta, Ti) compared to the Mesozoic (>107 Ma) magmatism (Sheldrick et al., 2018).

6.3. Mineral chemistry

Olivine ($n = 6$), clinopyroxene ($n = 7$), orthopyroxene ($n = 1$) and plagioclase ($n = 10$) phenocrysts in samples from Khukh Tolgoi and Samaan Damba areas underwent microprobe analysis. We report these analyses and methodology in the online supplementary material.

Olivine phenocryst cores were carefully analysed to best avoid areas that were altered to iddingsite and forsterite contents range from Fo56 to Fo66 for Khukh Tolgoi samples and Fo60 to Fo77 for Samaan Damba samples (Fig. 9a). Plagioclase feldspar compositions straddle the boundary between andesine and labradorite in composition (Fig. 9b). The analysed clinopyroxene phenocrysts are augites, and the single orthopyroxene xenocryst in sample KT4 from Khukh Tolgoi is an enstatite (Fig. 9c).

7. Data interpretation

7.1. Fractional crystallization

The low to moderate Mg-numbers (Fig. 7) indicate that none of these melts are primary. Olivine phenocrysts were identified in samples from all localities (Fig. 4), and the positive correlation between Mg-number and Ni for Khukh Tolgoi and Samaan Damba samples likely reflects olivine fractionation (Fig. 7f). Clinopyroxene phenocrysts were also identified during petrological studies, and the positive correlation between Mg-number and CaO/Al₂O₃ values, and chondrite-normalized Dy/Dy* [$\frac{Dy}{Dy^*} = \frac{Dy_n}{La_n^{4/13} Yb_n^{9/13}}$; Davidson et al., 2012] values, is consistent with clinopyroxene fractionation (Fig. 7e & i). Amphibole was not observed during petrological studies and Dy/Yb ratios do not vary with Mg-number, consistent with insignificant amphibole fractionation (Fig. 7j). Chondrite-normalized Eu/Eu* numbers [$\frac{Eu}{Eu^*} = \frac{Eu_n}{((Sm_n + Gd_n)0.5)}$] range from 0.94 to 1.11 (Avg = 1) for Tsagaan Nuur, 0.98 to 1.35 (Avg = 1.05) for Khukh Tolgoi and 0.69 to 1.10 (Avg = 0.96) for the Samaan Damba Area samples. Thus, samples have Eu/Eu* values close to 1 (Fig. 8; other than trachydacite sample SD12 from Samaan Damba), which indicates insignificant plagioclase removal or accumulation. Petrological studies identified oxides from all samples localities, and the positive correlation between Mg-number and Fe₂O_{3(T)}, Cr and primitive mantle-normalized Ti/Ti* [$\frac{Ti}{Ti^*} = \frac{Ti_n}{((Sm_n + Gd_n) + (Tb_n))}$; Davidson et al., 2012] values further support fractionation of Ti-bearing Fe-oxides (Fig. 7c & g–h).

7.2. Crustal contamination

Despite our samples being variably evolved, the lack of crustal xenoliths is not consistent with significant crustal assimilation processes, and there is no correlation between Mg-number and ⁸⁷Sr/⁸⁶Sr_(t) (Fig. 10a). However, four samples from the Samaan Damba Area have negative εNd_(t) values and low Mg-numbers, which might indicate late-stage crustal contamination (Fig. 10b). All other samples have analogous εNd_(t) values at a given Mg-number. Our samples are comparable to Mesozoic lavas from the Gobi–Altai and eastern Mongolia (Fig. 10c), which were interpreted as melts from a metasomatized subcontinental lithospheric mantle (e.g., Dash et al., 2015; Sheldrick et al., 2018).

To assess whether crustal contamination of an asthenospheric melt could generate the Mesozoic samples isotopic composition we perform assimilation–fractional crystallization (AFC) modelling (Fig. 10c). We utilize sample TB95–7.1.6 from Tsost Magmatic Field as the starting composition (MgO = 6.3 wt%), because this sample is from the Gobi–Altai and derived from the asthenospheric mantle. Crustal xenolith compositions were reported by Barry et al. (2003) and we utilize a granodiorite crustal xenolith (TB95–2.5) from the Gobi–Altai Bogd Plateau as the contaminator. Furthermore, this granulite sample has some of the most extreme isotopic values reported by Barry et al.

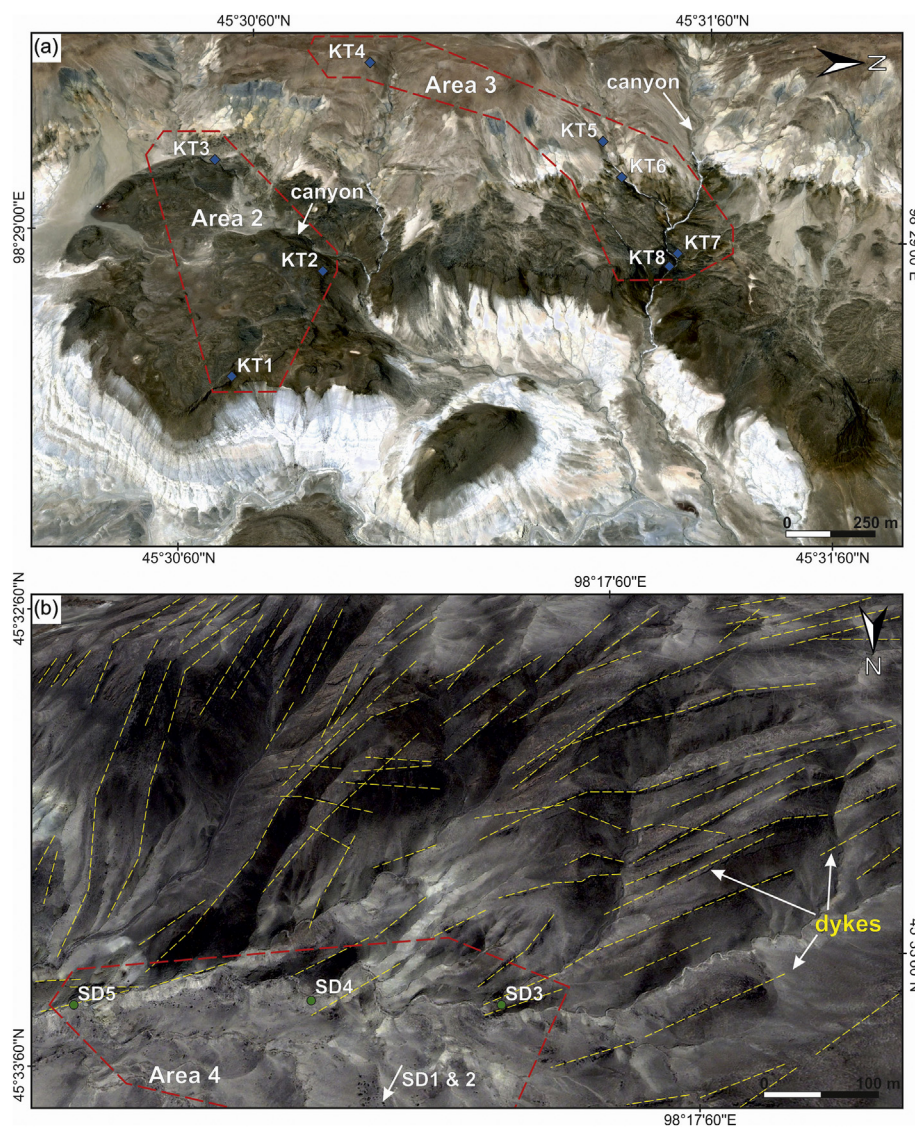


Fig. 2. a) Aerial view (Digital Globe, 2019) of basaltic flows from areas 2 and 3 showing a relatively compact volcanic stratigraphy of several individual flows up to 100 m thick, capping a white sedimentary sequence. b) Aerial view (Digital Globe, 2019) of a basaltic dyke swarm from Area 4. Dykes are emphasized by yellow dashed lines in this image. (For interpretation of the references to colour in this figure legend, the reader is referred to the web version of this article.)

(2003) and would therefore have the biggest effect on changing primary isotope compositions during AFC modelling. However, even utilizing high rates of assimilation (r -values of 0.4 and 0.8; Depaolo, 1981) we are unable to generate the full variety of isotopic compositions.

Overall, although it seems unlikely that the Mongolian lavas could have traversed through the continental crust without undergoing some crustal contamination, based on all the analysis above, crustal contamination processes seem to be less significant than source variation.

7.3. Thermobarometry modelling

7.3.1. Mineral-liquid thermobarometers

Here we use the analysed phenocryst compositions to estimate the pressure and temperature conditions of these fractionating phases (Fig. 11a-d).

Firstly, Equation 14 from Putirka (2008) is used to establish the thermometry of fractionating olivine phenocrysts, using the whole-rock composition of the phenocryst host rock to represent the liquid composition. This equation is applicable for any volcanic rock saturated with olivine and any other collection of phases, over a variety of pressure and temperature ranges (0.0001–14.4 GPa; 729–2000 °C; $\text{SiO}_2 =$

31.5–73.64 wt%; $\text{Na}_2\text{O} + \text{K}_2\text{O} = 0\text{--}14.3$ wt%; $\text{H}_2\text{O} = 0\text{--}18.6$ wt%) and has a standard error estimate (SEE) of 51 °C. Although care was taken to analyse the freshest olivine phenocrysts, this mineral has often undergone partial alteration to iddingsite. Therefore, a Rhodes diagram is utilized to test olivine-liquid equilibrium (Fig. 11a). If olivine crystals are in equilibrium with coexisting whole-rock compositions, then the putative liquid-olivine pair should plot along the solid line, or within established error bounds (Putirka, 2008). Only one analysed olivine phenocryst from Samaan Damba (SD3) plots within acceptable error and yielded a pressure-independent thermometry result of 1191 °C.

Care was taken to only analyse clinopyroxene phenocrysts that did not show any melt reaction textures, to reduce the risk of analysing antecrysts or xenocrysts. The clinopyroxene phenocrysts have low Al_2O_3 compositions and are similar in composition to experiments (LEPR# 3916–3917) in Villiger et al. (2004), which had clinopyroxene equilibration at ~10 kbar. As a test for clinopyroxene-liquid equilibrium, we plot the predicted clinopyroxene compositions against measured values (Fig. 11b), which has been shown as a good test for RIMG model applicability (Putirka, 2008). This model predicts the equilibrium values for the clinopyroxene components DiHd, EnFs, and CaTs, using experimental pressure/temperature data, and liquid compositions as

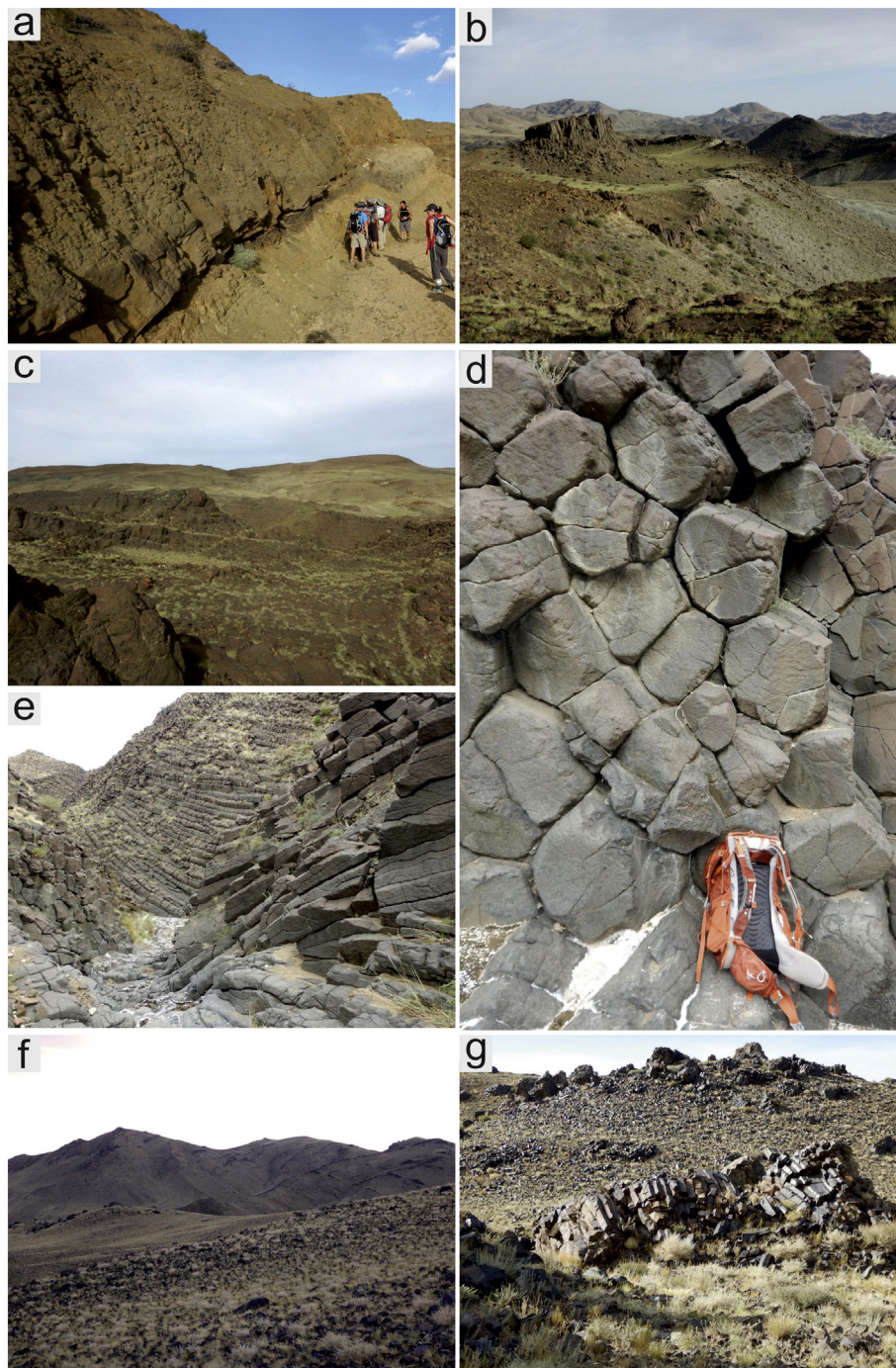


Fig. 3. a) 15 m thick lava flow sitting on a sedimentary breccia (debris flow) in Area 1 (Tsagaan Nuur). b) Remnant of a thick (~25 m) individual lava flow with columnar jointing at Area 2 (Khukh Tolgoi). c) Image of pahoehoe flows at Area 2. d) Distinctive columnar basalt with shallow dipping columns from Area 3 (Khukh Tolgoi). e) Columnar basalt with shallow dipping columns from Area 3. f) View of a basaltic dyke swarm in the background hill, from Area 4 (Samaan Damba area). g) Small-scale stock-like basaltic exposures in Area 4.

input. Our clinopyroxene compositions plot close to predicted values, suggesting that they were in equilibrium with the melt. However, the Putirka (2008) mineral-liquid thermobarometers requires sufficient Al_2O_3 in the clinopyroxene for calibrations to calculate a jadeite component. Therefore, we use a clinopyroxene-only thermometer model (RiMG) and use our plagioclase barometer results, which are discussed further below, as a model input. This model yields a temperature at which liquids will become saturated with clinopyroxene at a given pressure. Calibrations using this method calculated temperatures within \pm

50 °C error (Eq. 34, Putirka, 2008). This model outputted temperatures of 1184–1216 °C and 1221 °C for samples from Khukh Tolgoi and Samaan Damba areas, respectively (Fig. 11c).

Plagioclase phenocrysts were the least altered and using Eq. 23 (SEE = 33 °C) from Putirka (2008), gave temperature estimates of 1194–1232 °C and 1198–1204 °C for samples from Khukh Tolgoi and Samaan Damba areas, respectively (Fig. 11d). As a test for plagioclase-liquid equilibrium, these results can be compared to the temperature estimate for a given melt to reach plagioclase saturation (Putirka,

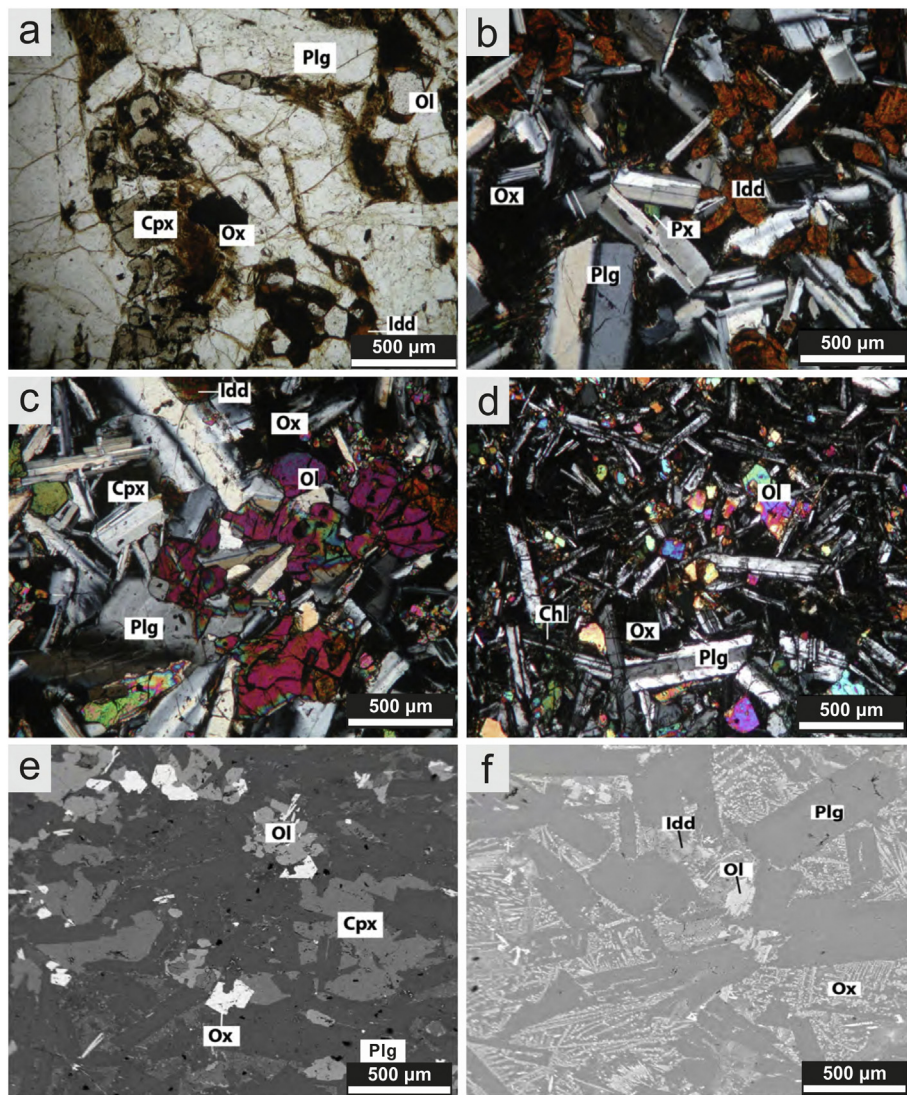


Fig. 4. Photomicrographs of Khukh Tolgoi Areas and Samaan Dyke Swarm. a) Large, euhedral, twinned, partly weathered plagioclase laths with numerous magnetite and ilmenite inclusions (Plain polarized light; KT8). Intergranular olivine crystals show variable degrees of weathering from alteration rims to complete pseudomorphism by iddingsite. b) Large, euhedral, twinned plagioclase laths with alteration patches and clusters of iddingsite pseudomorphs after olivine (Cross polarized light; KT3). Fe and Ti oxides appear as small discrete grains or as alteration products on pyroxenes. c) Cluster of euhedral, twinned, partly weathered plagioclase and anhedral, fractured olivine phenocrysts (crossed polarized light; KT5). Some olivine crystals are partly altered to iddingsite (red-brown in XPL). The opaque minerals are Fe and Ti oxides (magnetite and ilmenite). d) Euhedral plagioclase laths and anhedral olivine grains with partial chlorite and iddingsite alterations (crossed polarized light; SD3). e) Backscattered electron image (KT5) illustrating clinopyroxenes partially enclosed by larger plagioclase laths. f) Dendritic Fe–Ti oxides overgrowths on plagioclase crystals observed in backscattered electron image (KT7). (For interpretation of the references to colour in this figure legend, the reader is referred to the web version of this article.)

2005, 2008). Modelling of plagioclase saturated temperatures produced a similar overall temperature range of 1198–1238 °C (Eq. 26, Putirka, 2008). As discussed by Putirka (2008), the plagioclase Na–Ca exchange barometer ($SEE = 1.8$ kbar) needs to be used with caution because it has had variable success with experimental datasets. However, we achieved modelled results of 9.5–11.2 kbar and 9–10.8 kbar from Khukh Tolgoi and Samaan Damba areas, respectively (~30 km depth). Whole-rock sample compositions also plot next to the 9 kbar (± 1.5 kbar) cotectic on the CIPW diagram (Fig. 6c), in agreement with the modelled plagioclase Na–Ca exchange barometer results.

Overall, these different mineral-liquid thermobarometers have produced mutually supportive results and suggest that upwelling magma stalled and underwent fractional crystallization processes, before finally erupting further to surface.

7.3.2. Mg and Si whole-rock thermobarometry

The silica and magnesium activity whole-rock thermobarometry technique by Lee et al. (2009) recalculates primary magma

compositions by theoretically adding olivine to the whole-rock until equilibrium with a Fo90-rich mantle is attained. Lee et al. (2009) recommend using samples with >9 wt% MgO because evolved magmas have undergone complicated fractional crystallization processes, which makes recalculating primary magma compositions more difficult. Therefore, we use the most primitive Mesozoic and Cenozoic Mongolian basaltic samples to introduce less error during the fractional crystallization correction process.

Our Mesozoic samples from the Argalant Range have low MgO (<6.5 wt%) so we exclude them from this modelling. However, Cenozoic basaltic samples have higher MgO values (Barry et al., 2003; Hunt et al., 2012; Yarmolyuk et al., 2015 and references therein). Here, we do Mg and Si whole-rock thermobarometry modelling (Fig. 11e) using the least evolved Cenozoic samples (9–11 wt% MgO; Khangai Range Watershed, Lower Orkhon River, Tariat, Tariat-Goramsan Formation, and Togo) which have not undergone significant alteration (LOI values <0.7 wt%). Because this thermobarometry technique is unsuitable for olivine-free pyroxenite-derived melts it is important to consider their

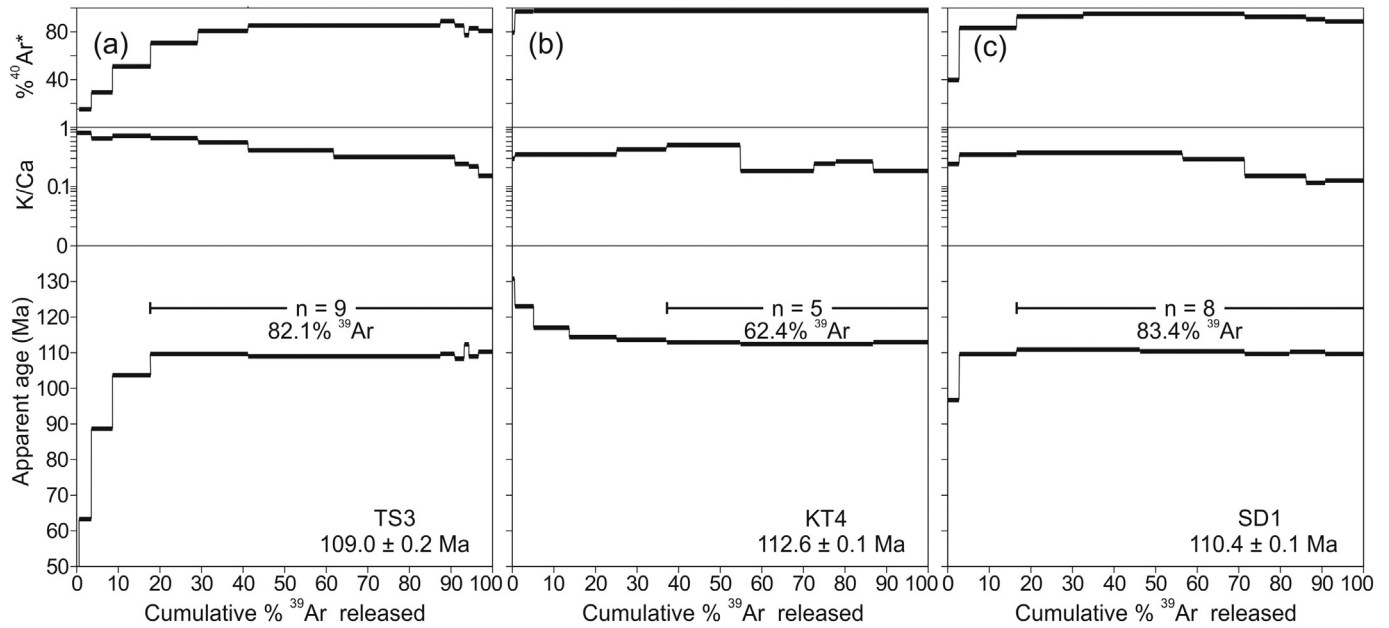


Fig. 5. Ar–Ar age plateau diagrams for Argalant Range samples. a) TS3 from Tsagaan Nuur. b) KT4 from Khukh Tolgoi. c) SD1 from Samaan Damba area.

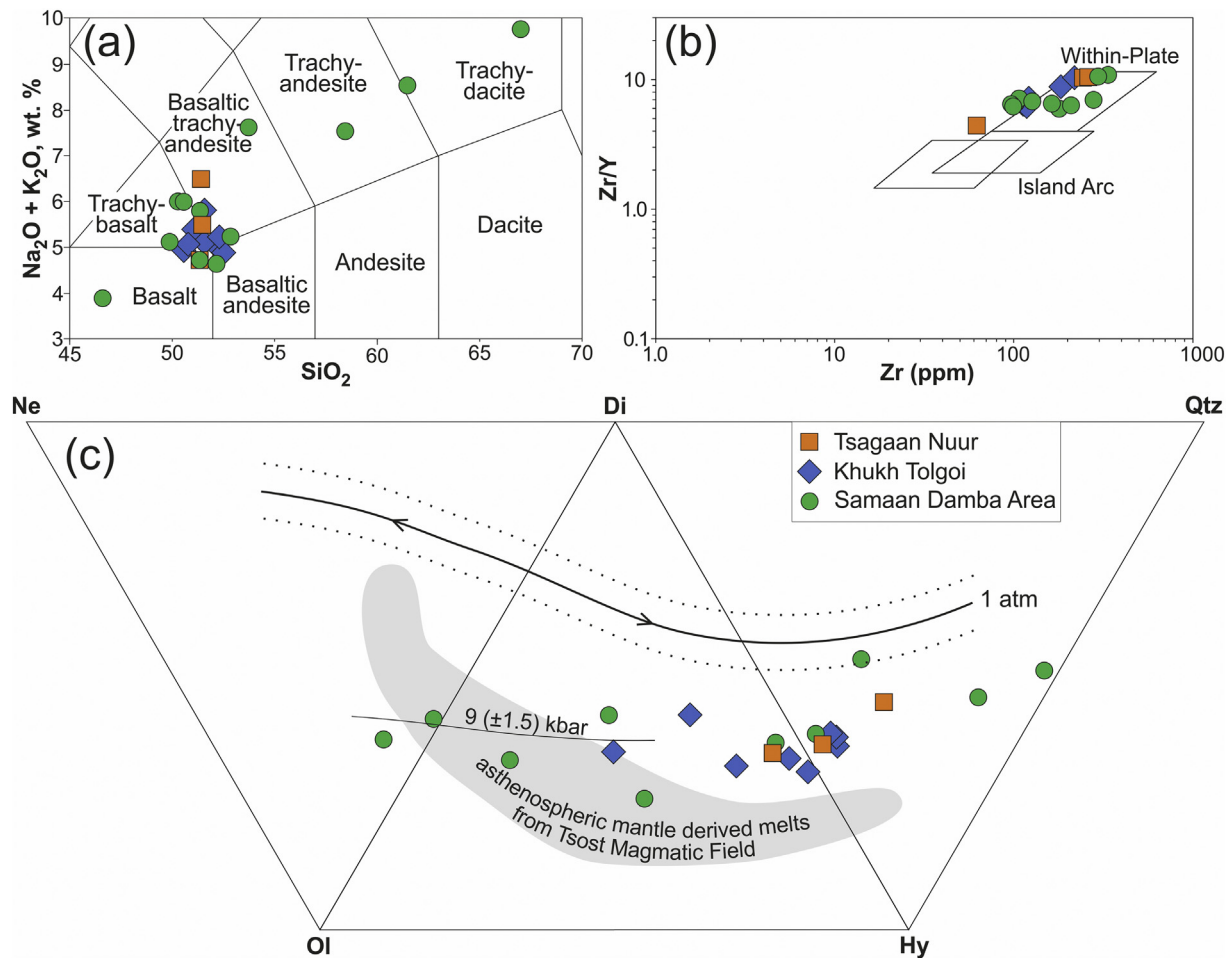


Fig. 6. a) An SiO_2 versus $\text{Na}_2\text{O} + \text{K}_2\text{O}$ (wt%) rock classification (TAS) plot. b) An immobile Zr versus Zr/Y (ppm) element tectonic discrimination diagram from Pearce and Norry (1979). c) Normative Ne-OI-Di-Hy-Qtz (CIPW) diagram calculated using $\text{Fe}_2\text{O}_3/\text{FeO}$ ratio of 0.2 ($\text{FeO} = \frac{\text{Fe}_2\text{O}_3}{1 + (\frac{\text{Fe}_2\text{O}_3}{\text{FeO}})}$) / 1.111 – sample SD12 excluded (trachy-dacite). The cotectics are from Thompson et al. (2001).

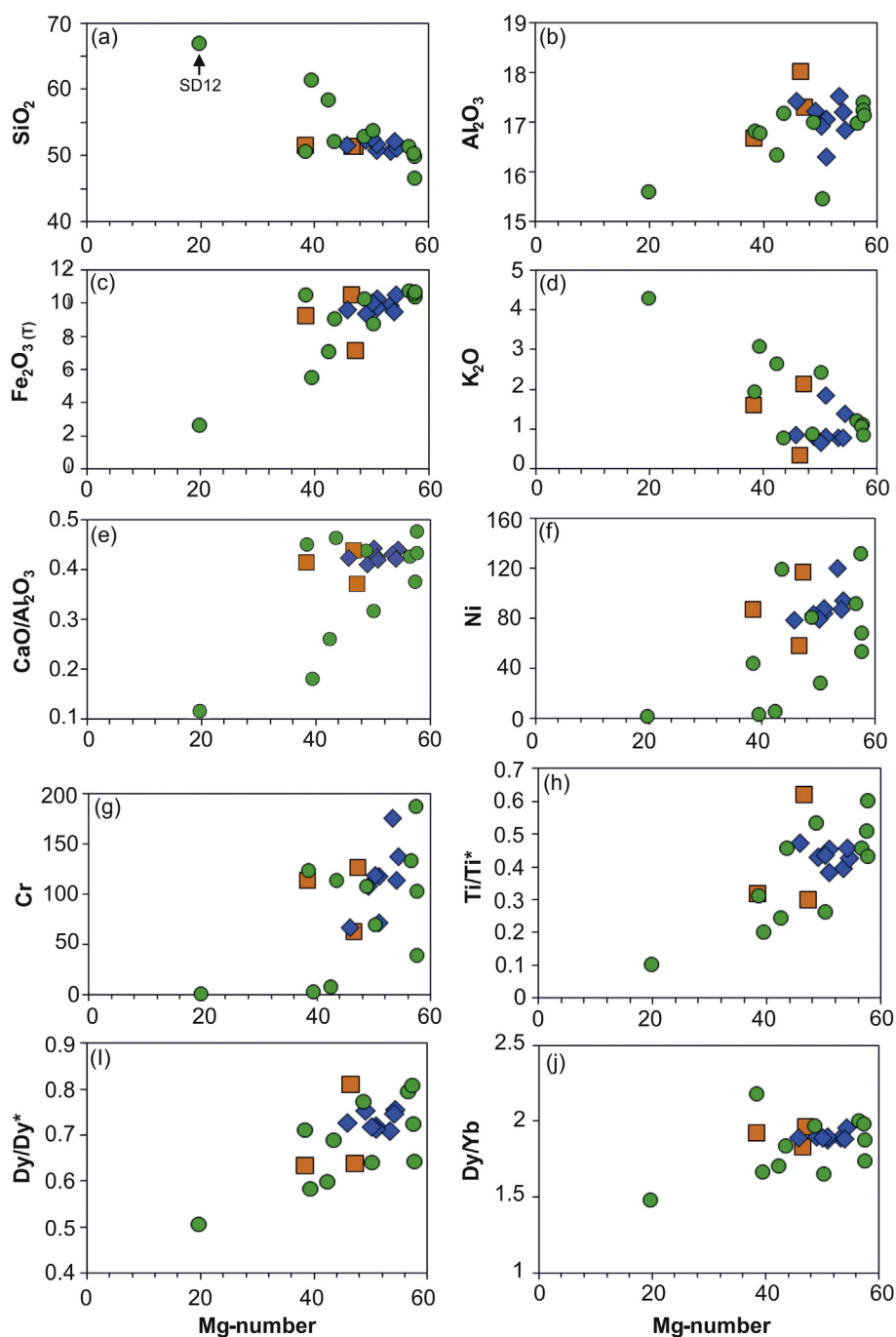


Fig. 7. Variations in major-element oxides (wt%), and compatible trace elements (ppm) with Mg-number (where Mg Number = $\left(100 \times \frac{\text{MgO}}{\frac{\text{MgO}}{40.3} + \frac{\text{FeO}}{71.85}}\right)$) is calculated using a $\text{Fe}_2\text{O}_3/\text{FeO}$ ratio of 0.2. The key is the same as in Fig. 6.

source characteristics (Lee et al., 2009). The Mongolian Cenozoic volcanism may be from a pyroxenite source, or contain significant pyroxenite components (Sheldrick et al., 2018) and we will further consider source composition in detail later. However, whatever the ultramafic source, if pyroxenite melts have equilibrated with an olivine-rich mantle, then this thermometer can be successfully applied (Ducea et al., 2013). Previous petrogenetic modelling on the Cenozoic volcanism utilized a peridotite source composition (Barry et al., 2003) or suggested the involvement of peridotite-like asthenospheric mantle (Sheldrick et al., 2020b), and therefore the Cenozoic magmatism likely interacted with, or was derived from, an olivine-bearing mantle.

For comparative purposes, we also include the three most primitive Mesozoic samples (>8 wt% MgO) from Tsost Magmatic Field in the Gobi-Altai (Fig. 1); these samples are basaltic dykes (LOI values ≤ 1.4 wt%) and derived from an olivine-rich asthenospheric mantle source (Sheldrick et al., 2018).

The Cenozoic samples have a range of calculated barometer (2.15–3.17 GPa) and thermometer (1404–1475 °C) results. For comparison, it is useful to compare our results with other tectonic/magmatic settings that have also used this thermobarometry technique. Modelling on MORB from the mid-Atlantic ridge and East Pacific Rise produced shallower and colder melts (Lee et al., 2009; 1300–1400 °C,

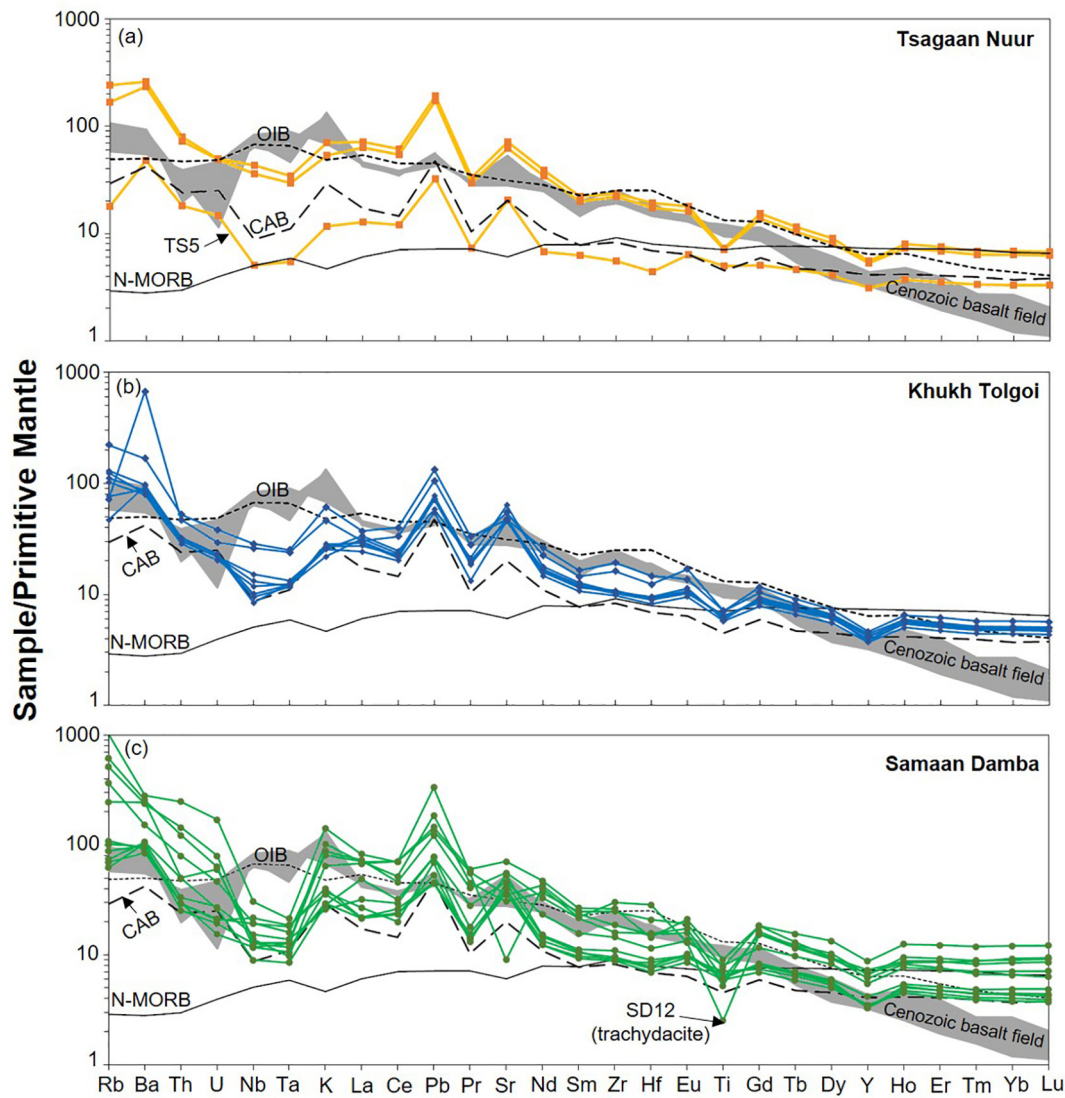


Fig. 8. Primitive mantle-normalized plots (Sun and McDonough, 1989). Data sources: average N-MORB: Gale et al. (2013); average OIB: Sun and McDonough; average CAB: Kelemen et al. (2003); Mongolian Cenozoic volcanism from the Gobi-Altai: Barry et al. (2003), Yarmolyuk et al. (2015) appendix material and references therein.

0.7–1.7 GPa). However, our thermobarometry results are generally lower than calculated Hawaiian “hotspot” volcanism (Lee et al., 2009; ~2–5 GPa, 1450–1600 °C), which is often interpreted to be from a deep thermal upwelling (e.g., mantle plume). Previous research has suggested that the Mongolian Cenozoic volcanism may be associated with a thermal anomaly, possibly due to the insulation effect of thick continental lithosphere (e.g., Barry et al., 2003) and/or that high temperatures are induced by mantle return flow in response to foundering ancient slabs (Sheldrick et al., 2020b). Interestingly, all samples from Togo plot across the fertile peridotite solidus (Hirschmann, 2000) which might advocate the involvement of non-peridotite components (Fig. 11e). These Togo samples have the highest calculated thermobarometry results, and any such pyroxenite melting may have occurred deeper, because pyroxenites melt 15–30 km deeper than peridotites along any given adiabat (e.g., Ducea et al., 2013). Alternatively, if the Togo samples were derived from an olivine-poor mafic source, then this silica and magnesium activity whole-rock thermobarometry technique may have over-estimated primary thermobarometry values and we will consider such a scenario more fully in the following sections.

Tsost Magmatic Field samples have lower barometer (1.62–1.66 GPa) and thermometer (1329–1330 °C) results. Magnesium and Si whole-rock thermobarometry modelling on the North American

Cordilla magmatism, in the Basin-and Range (USA), calculated similar thermobarometry values (~2 GPa, 1350–1450 °C) and attributed it to localized partial melting zones, in an area that has undergone rapid lithospheric thinning (Lee et al., 2009). The Gobi-Altai was an area of rapid lithospheric removal during the Mesozoic, and therefore a similar scenario might be plausible for Tsost Magmatic Field basalts.

7.4. Variations in trace-elements and major-elements to assess source petrogenesis

7.4.1. Trace-element variations

Olivine mineral chemistry can help assess magmatic processes because melts that incorporate pyroxenite/eclogite are expected to crystallize olivine with high Ni and low Ca compared to melts of pure peridotite (Herzberg et al., 2014; Sobolev et al., 2007). Therefore, we use our olivine phenocryst geochemical data to help assess magmatic processes (Fig. 12a-b). Because any simultaneous fractional crystallization of minerals other than olivine will alter olivine chemistry, we incorporate calculated liquid lines of descent (LLD) from Herzberg et al. (2014) onto Fig. 12a-b. These calculated LLD used a primary magma which was sourced from a peridotite-dominated lithology with pyroxenite components. Our olivine compositions are comparable to those

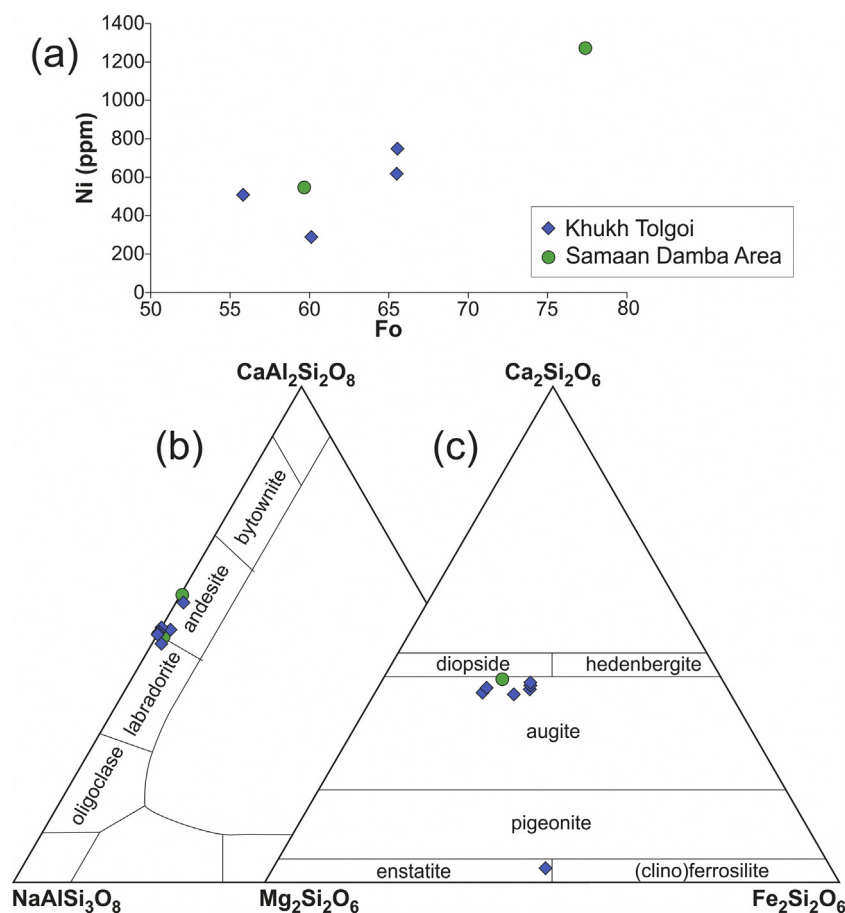


Fig. 9. a) Olivine forsterite versus Ni (ppm). b) Plagioclase feldspar An-Ab-Or composition plot. c) Pyroxene $\text{Ca}_2\text{Si}_2\text{O}_6$ - $\text{Mg}_2\text{Si}_2\text{O}_6$ - $\text{Fe}_2\text{Si}_2\text{O}_6$ composition plot.

from Mangaia which are interpreted by Herzberg et al. (2014) to require pyroxenite in the source (Fig. 12a-b), having higher Ni and lower Ca than pure peridotite melts.

We will now consider whole-rock Zn/Fe and Mn/Fe ratios to evaluate differences in source lithology between the Mongolian Mesozoic and Cenozoic magmatism. However, because residual garnet in the source rock can elevate these ratios, it is useful to first consider variations in the garnet signature between sample localities. Because Yb is highly compatible in garnet but not clinopyroxene, we use primitive mantle-normalized $\text{Sm}/\text{Yb}_{(n)}$ vs. $\text{Dy}/\text{Yb}_{(n)}$ ratios to assess changes in the garnet signature (Fig. 12c). To help with this assessment and future discussion, it is useful to also include existing data on Mesozoic asthenospheric mantle-derived basalts from Tsost Magmatic Field, and existing data on the Cenozoic lavas (Gobi-Altai; Khangai Range Watershed, Tariat, Tariat-Goramsan Formation, and Togo). Mesozoic samples have lower $\text{Sm}/\text{Yb}_{(n)}$ vs. $\text{Dy}/\text{Yb}_{(n)}$ values than the Cenozoic samples and this might indicate that the Mesozoic magmatism was derived from a less-rich garnet-bearing source lithology.

Because Zn is more incompatible than Fe in garnet and clinopyroxene ($K_{D(\text{Cpx})}^{\text{Zn}} K_{D(\text{Grt})}^{\text{Zn}} \leq 1$), but partitions equally between olivine and orthopyroxene under mantle conditions ($K_{D(\text{Oli})}^{\text{Zn}} K_{D(\text{Opx})}^{\text{Zn}} = 0.9-1$), high Zn/Fe ratios have been utilized to identify pyroxenite versus peridotite sources (Le Roux et al., 2010; a pyroxenite source can generate Zn/Fe $\times 10^4$ ratios as high as ~14, at 12 MgO wt%, or even higher if the source is garnet-rich). Alternatively, high Zn/Fe ratios can be generated through Zn-enrichment, due to metasomatism processes, and

thus help identify metasomatized source components. Our samples trend towards increasing Zn/Fe ratios with decreasing MgO indicative of fractional crystallization processes (Fig. 12d). Nevertheless, these samples have high Zn/Fe ratios compared to Tsost Magmatic Field basalts, which were derived from an asthenospheric mantle peridotite-like lithology (Sheldrick et al., 2018). The similar $\text{Sm}/\text{Yb}_{(n)}$ and $\text{Dy}/\text{Yb}_{(n)}$ ratios between Tsost Magmatic Field basalts and our Mesozoic samples indicates that this Zn/Fe variation is unlikely to be due to garnet (Fig. 12c) – although clinopyroxene fractionation would have likely increased Ze/Fe ratios. Therefore, the high Zn/Fe values in our Mesozoic samples likely reflects clinopyroxene fractionation and previous Zn-enriching source metasomatism processes and/or mafic source components. The Cenozoic samples also have high Zn/Fe ratios, with some samples from Tariat plotting outside the peridotite melting zone at >10 wt% MgO and all samples having much higher Zn/Fe ratios than Tsost Magmatic Field basalts. However, it is interesting to note that at >8 wt% MgO, many Cenozoic samples plot in the peridotite-melting zone (note, this zone still encompasses pyroxenite melting), perhaps advocating the involvement of olivine-rich source components in melt generation (e.g., peridotite/olivine-rich pyroxenite). Furthermore, any residual garnet in the Cenozoic magmatic source may have elevated Zn/Fe ratios in the melt. For comparison, we further compare our samples to Cenozoic magmatism from the NCC (Fig. 1), which was interpreted to be derived from a clinopyroxene/garnet-rich mantle source (Liu et al., 2008, and references therein). This NCC magmatism has similar Zn/Fe ratios to the Mongolian Cenozoic magmatism, perhaps indicating broadly similar source lithologies between the Mongolian and NCC Cenozoic magmatism.

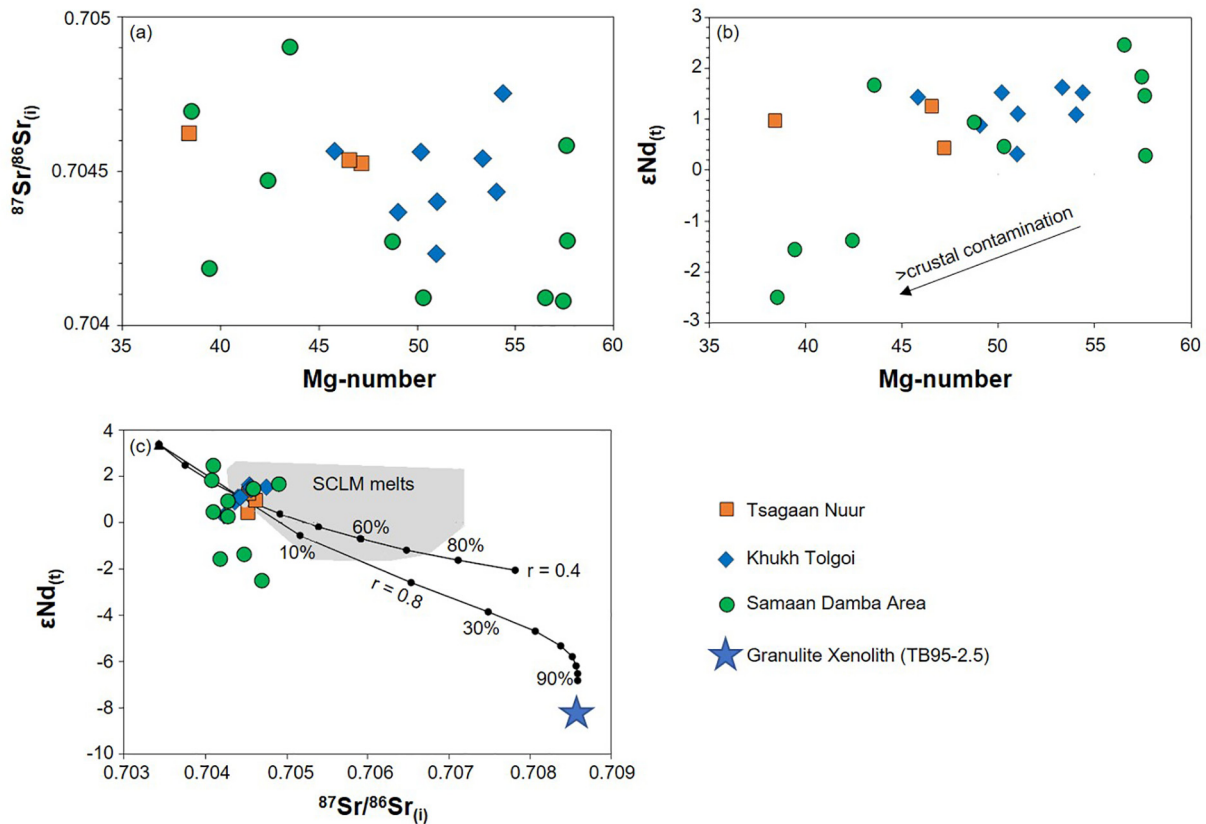


Fig. 10. a) Mg-number versus $^{87}\text{Sr}/^{86}\text{Sr}_{(i)}$, b) Mg-number versus $\epsilon\text{Nd}_{(t)}$, c) $^{87}\text{Sr}/^{86}\text{Sr}_{(i)}$ versus $\epsilon\text{Nd}_{(t)}$. The solid lines show AFC modelling results (equations from Depaolo, 1981) and the contaminator used was a granulite crustal xenolith (TB95–2.5) from the Gobi-Altai Bogd Plateau (Barry et al., 2003). The amount of F (mass of magma/initial mass of magma) ranges from 1 to 0.1 and tick marks are in 10% intervals. Two different r -values (assimilation against fractionation rate) of 0.4 and 0.8 was utilized. Sample SD12 (trachydacite) not plotted due to out of range scale bar (Mg-number = 19.75, $^{87}\text{Sr}/^{86}\text{Sr}_{(i)}$ = 0.6992, $\epsilon\text{Nd}_{(t)}$ = -1.94). Sr and Nd initial isotope ratios calculated using: Tsagaan Nuur = 109 Ma, Khukh Tогоi = 113 Ma, and Samaan Damba = 110 Ma.

Whole-rock Fe/Mn ratios can also be used to assess the relative contributions of peridotite and pyroxenite source lithology. This is because olivine has a relatively high Fe/Mn concentration compared to clinopyroxene and orthopyroxene. Therefore, melting of an olivine-rich mantle should have an enriched Fe/Mn ratio. Le Roux et al. (2010) set a range on the Fe/Mn ratio during peridotite melting, using samples with >8.5 wt% MgO (Fig. 12d). However, late-stage fractionation of minerals such as clinopyroxene and plagioclase will also change this ratio. Most of the Mesozoic and Cenozoic samples plot in the peridotite melting field – with our olivine phenocryst data also having similar Fe/Mn ratios (55–70) – advocating the melting or assimilation of an olivine-bearing source lithology. The Cenozoic magmatism from the NCC also has whole-rock Fe/Mn ratios that mostly plot within, or just above ($\text{Fe}/\text{Mn} \geq 74$), the peridotite melting field.

7.4.2. Major-element variations

Whole-rock melting experiments of peridotite and pyroxenite compositions were used by Yang and Zhou (2013) to generate a FC3MS ($\text{FeO}_{(T)}/\text{CaO} - 3 \times \text{MgO}/\text{SiO}_2$ wt%) parameter to help distinguish between peridotite and mafic (pyroxenite/hornblende) sources. High FC3MS values are typically attributed to a mafic source and modelling done by Yang and Zhou (2013) indicates that the highest FC3MS value that can be produced from peridotite melting is 0.65 when MgO is >7.5 wt%. This parameter is primarily controlled by source composition and melting degree, while pressure and temperature has little effect. Clinopyroxene fractionation will also increase FC3MS values and therefore we utilize a MgO versus FC3MS plot to help assess source controls (Fig. 13a). Using FC3MS values it is difficult to assess peridotite versus pyroxenite components for our Mesozoic samples because of fractional

crystallization processes. However, the Cenozoic samples from the Khangai Range Watershed, Tariat and Togo at >7.5 wt% MgO have FC3MS values >0.65 , indicating that these are unlikely to be derived from a pure peridotite source. The Cenozoic magmatism from the North China Craton also has high FC3MS values, comparable to the Mongolian Cenozoic magmatism. However, some of the NCC Cenozoic magmatism from Caiyuan (Liaoning) has low FC3MS values (0.24–0.28) at 8–10 wt% MgO. Furthermore, these Caiyuan samples also have comparatively low Zn/Fe ratios (9–12) which might indicate that this magmatism was derived from a more olivine-rich mantle source or assimilated an olivine-rich mantle.

Discriminant functional analysis and multivariate regression was performed on mantle-like lherzolites and pyroxenites to develop different parameters to help constrain source lithology (Yang et al., 2019). The FCKANTMS parameter [$\text{FCKANTMS} = \ln(\text{FeO}_{(T)}/\text{CaO}) - 0.08 \times \ln(\text{K}_2\text{O}/\text{Al}_2\text{O}_3) - 0.052 \times \ln(\text{TiO}_2/\text{Na}_2\text{O}) - 0.036 \times \ln(\text{Na}_2\text{O}/\text{K}_2\text{O}) \times \ln(\text{Na}_2\text{O}/\text{TiO}_2) - 0.062 \times (\ln(\text{MgO}/\text{SiO}_2))^3 - 0.641 \times (\ln(\text{MgO}/\text{SiO}_2))^2 - 1.871 \times \ln(\text{MgO}/\text{SiO}_2) - 1.473$] was devised to recognize the compositional difference between melts of pyroxenite-like and lherzolite compositions. The incorporation of selected log-ratios into this FCKANTMS parameter was shown by Yang et al. (2019) to significantly reduce temperature and pressure controls on calculated values. Because late-stage fractional crystallization controls will alter FCKANTMS values we use a MgO versus FCKANTMS plot to aid interpretations (Fig. 13b). Because our Mesozoic samples have relatively low MgO, their calculated FCKANTMS values will not reflect primary melt compositions. Nevertheless, our samples have much higher FCKANTMS values than all the peridotite melting experiments at comparable MgO concentrations. Tsost Magmatic Field samples also have lower FCKANTMS values at a

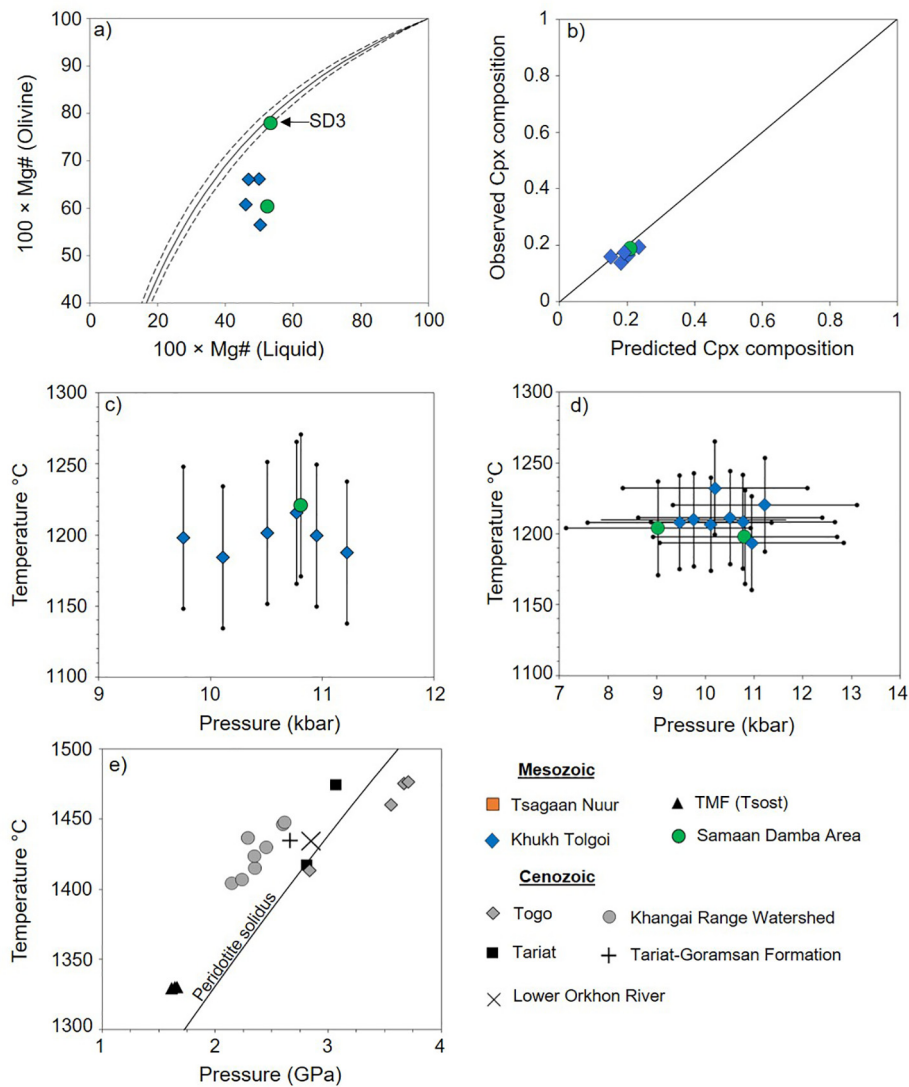


Fig. 11. a) Rhodes diagram testing for olivine-liquid equilibrium. The dotted lines represent established error boundaries, here given as $K_D(\text{Fe}-\text{Mg})^{\text{Oliv-Liq}} = 0.30 \pm 0.03$ (Putirka, 2008). b) Predicted clinopyroxene composition versus observed clinopyroxene compositions. c) Calculated clinopyroxene thermometry results. d) Calculated plagioclase feldspar thermometry and barometry results. Error bars represent established standard error estimates (Putirka, 2008). e) Whole-rock Mg and Si barometer versus whole-rock thermometry results. Sample data from Barry et al. (2003), Hunt et al. (2012), Yarmolyuk et al. (2015) appendix material and references therein, and Sheldrick et al. (2018).

given MgO concentration compared to all other sample localities, likely indicating a more olivine-rich mantle source lithology. Cenozoic lavas also have higher FCKANTMS values than all the peridotite melting experiments and sample localities exhibit a bell-shaped curve likely due to fractional crystallization processes, or possibly because of later-stage olivine assimilation into a melt (increasing MgO and decreasing FCKANTMS values). If we just consider the Cenozoic samples with >10 wt% MgO, it suggests that samples from Togo require the most pyroxenite-like (mafic) material, followed by Tariat and finally Khangai Range Watershed. The Cenozoic magmatism from the NCC also has high FCKANTMS values. However, magmatism from Caiyuan (Liaoning) has comparatively low FCKANTMS values (0.15–0.24), comparable to Mesozoic samples from Tsost Magmatic Field.

Using PRIMELT3 MEGA (Herzberg and Asimow, 2015) we calculate a more primary melt composition for samples with >8 wt% MgO (Tsost Magmatic Field and Cenozoic lavas). This software is used as a calculator for olivine liquid line of descent and can be applied to a basalt from a pyroxenite source. We also include a calculated curve using this software showing olivine being incrementally added in 1% intervals (up to 12%) and highlights how any olivine assimilation would lower FCKANTMS

values (Fig. 13b). However, even by “adding” olivine to the Cenozoic samples, producing theoretical whole-rock compositions >16 wt% MgO, some samples still have FCKANTMS values >0.37 , which has been suggested as the upper bound for peridotite melting (Yang et al., 2019).

Another method to discriminate between mafic and olivine-rich mantle sources is to combine FCKANTMS with $\ln(\text{SiO}_2/(\text{CaO} + \text{Na}_2\text{O} + \text{TiO}_2))$ values (Fig. 13c). This method has been able to distinguish between mafic and peridotite sources (Yang et al., 2019). Here we plot the Mesozoic and Cenozoic samples on a $\ln(\text{SiO}_2/(\text{CaO} + \text{Na}_2\text{O} + \text{TiO}_2))$ vs. FCKANTMS plot and include the experimental melt data used in Yang et al. (2019) for comparative purposes. The Mesozoic and Cenozoic samples plot outside the peridotite and harzburgite fields, and instead plot in the transitional melt zone or in the mafic-melts field. However, clinopyroxene and plagioclase fractionation will increase FCKANTMS values and therefore it is likely that the Mesozoic samples, and the most evolved Cenozoic samples, have a more “mafic” signature on this plot, due to the fractionation of these phases. Cenozoic samples from the NCC mostly plot in the mafic-melts field, although samples from Caiyuan (Liaoning) plot in the transitional field.

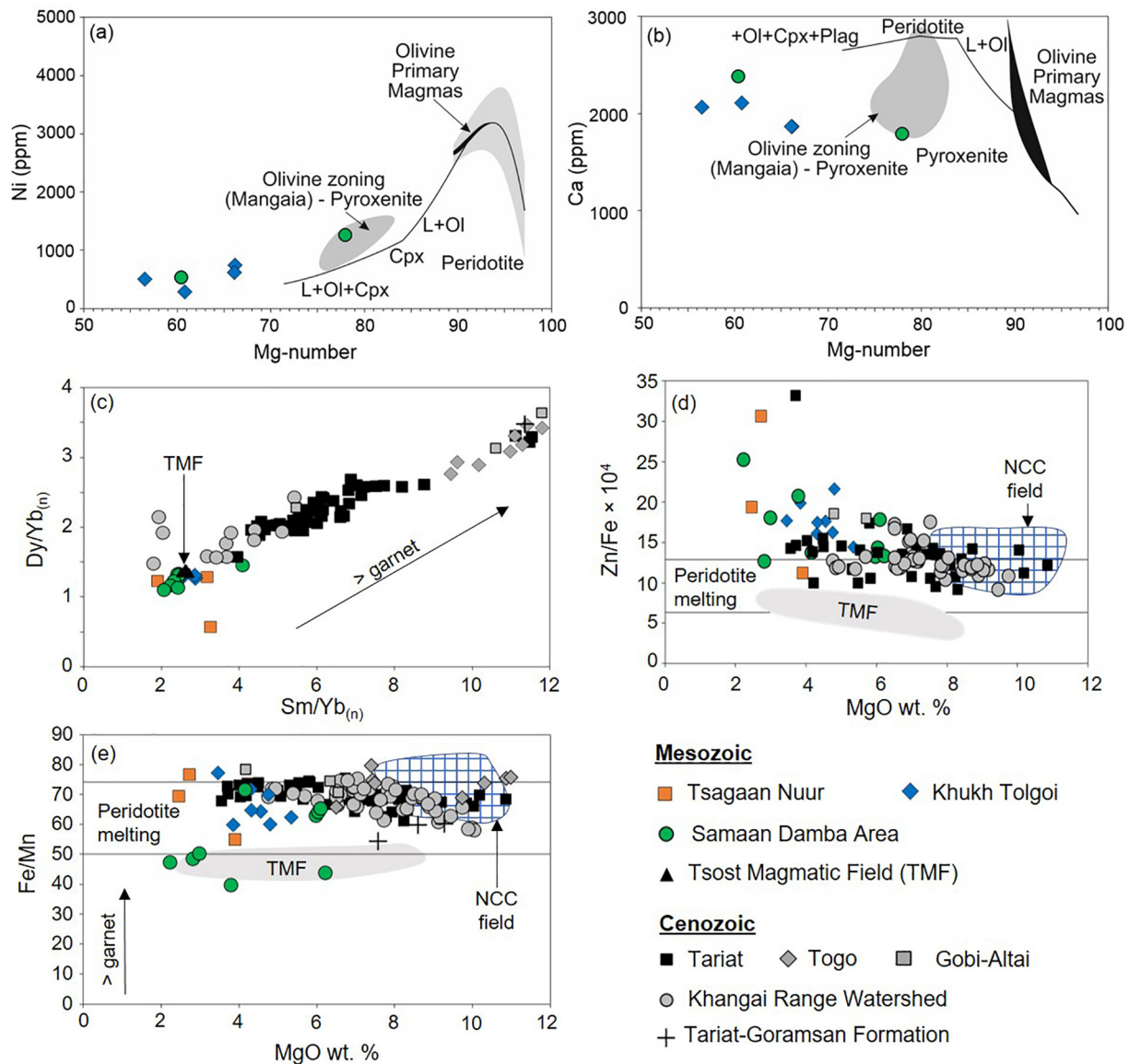


Fig. 12. a) Olivine Mg-number versus Ni compositions for Khukh Tolgoi and Samaan Damba samples. Calculated liquid lines of descent and zoned olivine “pyroxenite” field from Herzberg et al. (2014). b) Olivine Mg-number versus Ca compositions for Khukh Tolgoi and Samaan Damba samples. c) Primitive mantle-normalized Sm/Yb_(n) versus Dy/Yb_(n) plot. d) MgO versus Zn/Fe × 10⁴. The peridotite melts field is based on information in Le Roux et al. (2010), however evolved samples which have undergone clinopyroxene fractionation will plot outside this field. TMF = Tsost Magmatic Field samples. e) MgO versus Fe/Mn plot, and the peridotite melts field is based on information in Le Roux et al. (2010). Additional data from: Barry et al. (2003), Hunt et al. (2012), Yarmolyuk et al. (2015) and references therein, and Sheldrick et al. (2018). Cenozoic North China Craton Field (n = 29) from Liu et al. (2008) and references therein. Trachydacite samples SD10 and SD12 excluded from plots.

8. Discussion

The Tsagaan Nuur, Khukh Tolgoi, and the Samaan Damba samples have geochemical signatures unlike asthenospheric mantle-derived basalts from Tsost Magmatic Field (i.e., depletion of some HFSEs such as Nb, Ta and Ti, and higher ⁸⁷Sr/⁸⁶Sr_(t) and lower εNd_(t) values), and instead probably reflect melts from metasomatized SCLM, which is similar to Mesozoic volcanism elsewhere in Mongolia (e.g., Dash et al., 2015). Previous ocean closure events (e.g., the closure of the Mongol-Okhotsk Ocean) would have provided opportunity to metasomatize the lithospheric mantle under Mongolia.

Whole-rock and mineral geochemistry results suggest that Tsagaan Nuur, Khukh Tolgoi, and the Samaan Damba samples are unlikely to be pure peridotite melts and instead require minor input from more mafic components (Figs. 12 & 13). However, due to the evolved nature of our Mesozoic samples, assessing the relative contributions of peridotite vs. pyroxenite is challenging. Future

studies would benefit from the application of non-traditional isotopes and additional mineral chemistry data to evaluate source lithology in further detail. Furthermore, it is unclear to what extent carbonate metasomatism processes may have changed the lithosphere under East Asia and influenced magmatic geochemical signatures (Nikolenko et al., 2020). Many studies indicate that during the Mesozoic there was large-scale lithospheric removal and asthenospheric mantle input across East Asia (e.g., Dash et al., 2015; Ma et al., 2016; Sheldrick et al., 2020b). However, asthenospheric mantle-derived basalts from Tsost Magmatic Field have geochemical signatures indicative of a more peridotite-like source component. Thus, although the volcanism from our field localities likely reflect SCLM + asthenospheric mantle input, the non-peridotite geochemical signatures are likely from a metasomatized SCLM component. We hypothesize that this metasomatized SCLM contained abundant pyroxenite veins which formed from previous melt reactions during the closure of the Mongol-Okhotsk Ocean.

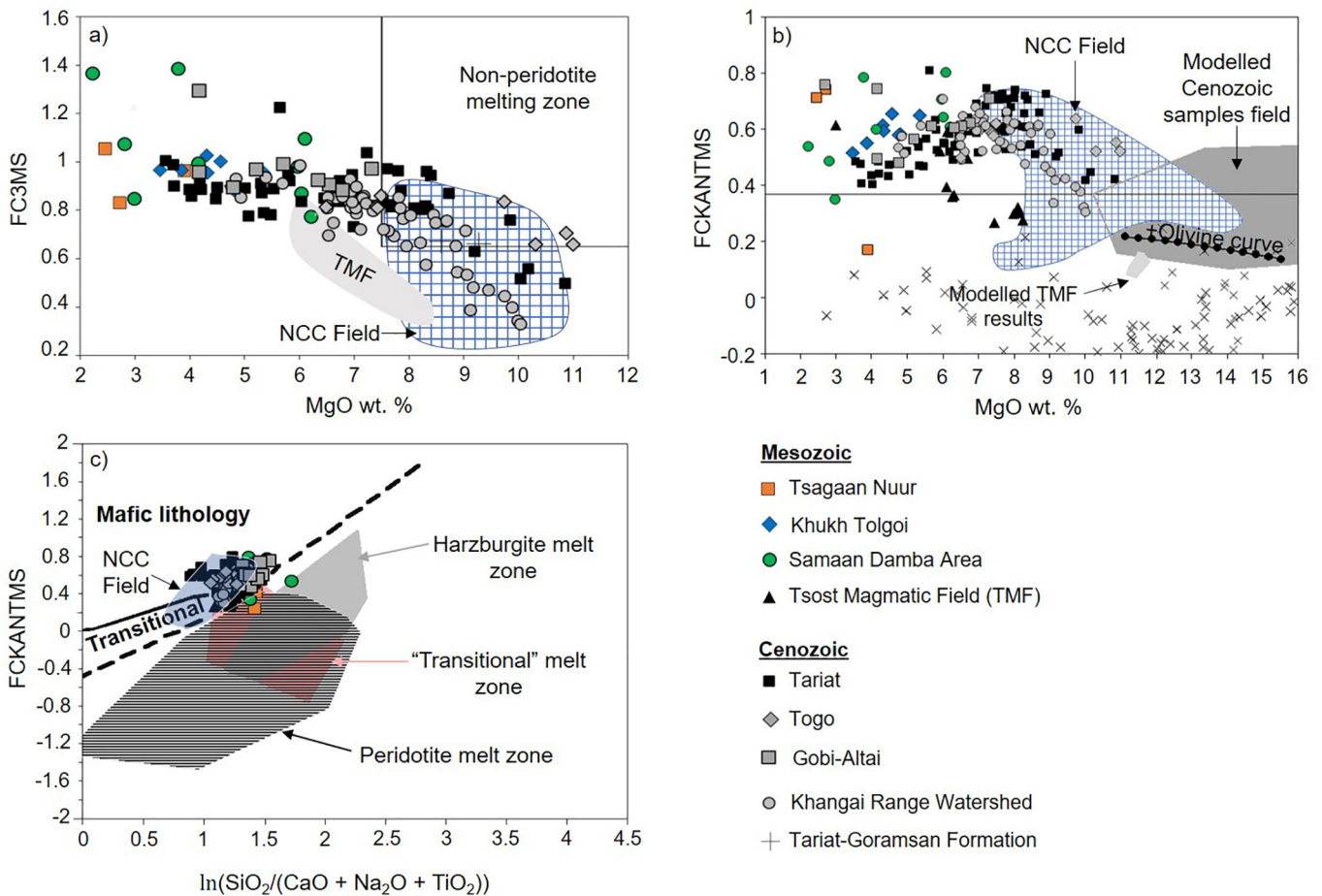


Fig. 13. Plots of: a) MgO versus FC3MS ($\text{FeO}_{\text{TOT}}/\text{CaO} - 3 \times \text{MgO}/\text{SiO}_2$ wt%). b) MgO versus FCKANTMS [$\ln(\text{FeO}_{\text{TOT}}/\text{CaO}) - 0.08 \times \ln(\text{K}_2\text{O}/\text{Al}_2\text{O}_3) - 0.052 \times \ln(\text{TiO}_2/\text{Na}_2\text{O}) - 0.036 \times \ln(\text{Na}_2\text{O}/\text{K}_2\text{O}) \times \ln(\text{Na}_2\text{O}/\text{TiO}_2) - 0.062 \times (\ln(\text{MgO}/\text{SiO}_2))^3 - 0.641 \times (\ln(\text{MgO}/\text{SiO}_2))^2 - 1.871 \times \ln(\text{MgO}/\text{SiO}_2) - 1.473$]. The solid line represents the upper bound on peridotite melting (FCKANTMS = 0.37) and is based on information in Yang et al. (2019). The little black crosses are reported peridotite melting experiments from Yang et al. (2019) appendix material. Olivine “addition” curve calculated using PRIMELT3 MEGA (Herzberg and Asimow, 2015); olivine added in 1% increments, until 12%. c) $\ln(\text{SiO}_2/(\text{CaO} + \text{Na}_2\text{O} + \text{TiO}_2))$ versus FCKANTMS. Peridotite melt zone, harzburgite melt zone and transitional melt zone based on information in Yang et al. (2019). Additional data from: Barry et al. (2003), Hunt et al. (2012), Yarmolyuk et al. (2015) and references therein, and Sheldrick et al. (2018). Cenozoic North China Craton Field ($n = 31$) from Liu et al. (2008) and references therein. Trachydacite samples SD10 and SD12 excluded from plots.

The Mongolian Cenozoic volcanism has geochemical signatures consistent with the melting of non-peridotite lithologies (Figs. 12 & 13). However, due to high Fe/Mn ratios, and samples plotting in the “transitional melt zone” on a $\ln(\text{SiO}_2/(\text{CaO} + \text{Na}_2\text{O} + \text{TiO}_2))$ vs. FCKANTMS plot, it indicates that this mafic source was likely olivine-rich (e.g., olivine-rich pyroxenite). This magmatism may have also incorporated olivine-rich lithologies into the melt. Spinel-peridotite xenoliths from the Tariat region (Carlson and Ionov, 2019) suggest an olivine-rich shallow lithospheric mantle under Mongolia; any such mantle may have been mixed and assimilated into upwelling magma. We note that this mafic signature exists in the Cenozoic magmatism from the NCC too, in agreement with conclusions from other researchers (e.g., Liu et al., 2008).

What processes triggered widespread Mesozoic and Cenozoic volcanism across East Asia is highly debated (Menzies et al., 2007). Nevertheless, models tend to converge on themes of interactions between subducted slabs and upwelling magma by either a cogenetic link with convective erosion above subducted Mongol-Okhotsk, Paleo-Pacific, and Paleo-Asian slabs (He, 2014; Windley et al., 2010), Paleo-Pacific slab roll-back, or delamination due to thermo-chemical weakening of the lithospheric mantle (e.g., Dash et al., 2015; Windley et al., 2010). Previous models invoking a mantle plume(s) (Yarmolyuk et al., 2015) to explain East Asian

magmatism is inconsistent with helium isotope studies on Cenozoic basalts (Barry et al., 2007). Furthermore, this mantle plume model has an age progression hypothesis inconsistent with the widespread East Asian magmatism (e.g., Dash et al., 2015; Sheldrick et al., 2018, 2020a-b), and inconsistent with East Asian tectonic plate reconstructions (e.g., Van der Voo et al., 2015).

We suggest that the Tsagaan Nuur, Khukh Tolgoi and Samaan Damba magmatism was triggered by piecemeal delamination (Fig. 14a) which was facilitated by previous compressional events associated with the closure of the Mongol-Okhotsk Ocean. Convective erosion of the lithosphere from upwelling asthenospheric mantle may have also assisted lithospheric removal processes. We note that this Mesozoic magmatism does not have a strong garnet signature, which likely reflects that at the time of magmatism, the SCLM had nearly been stripped away and therefore less involvement from any residual garnet (e.g., Sheldrick et al., 2018). Given the large distance between the Argalant range and the Paleo-Pacific slab, it is unclear whether this large-scale tectonic system could have facilitated Mesozoic magmatism in western Mongolia. Given the striking geochemical similarities between the Mongolian and North China magmatism, detailed numerical studies are now required to test to what extent the Paleo-Pacific slab had in removing the East Asian lithospheric root (Wang et al., 2017; Liu et al., 2019, Sheldrick et al., 2020b).

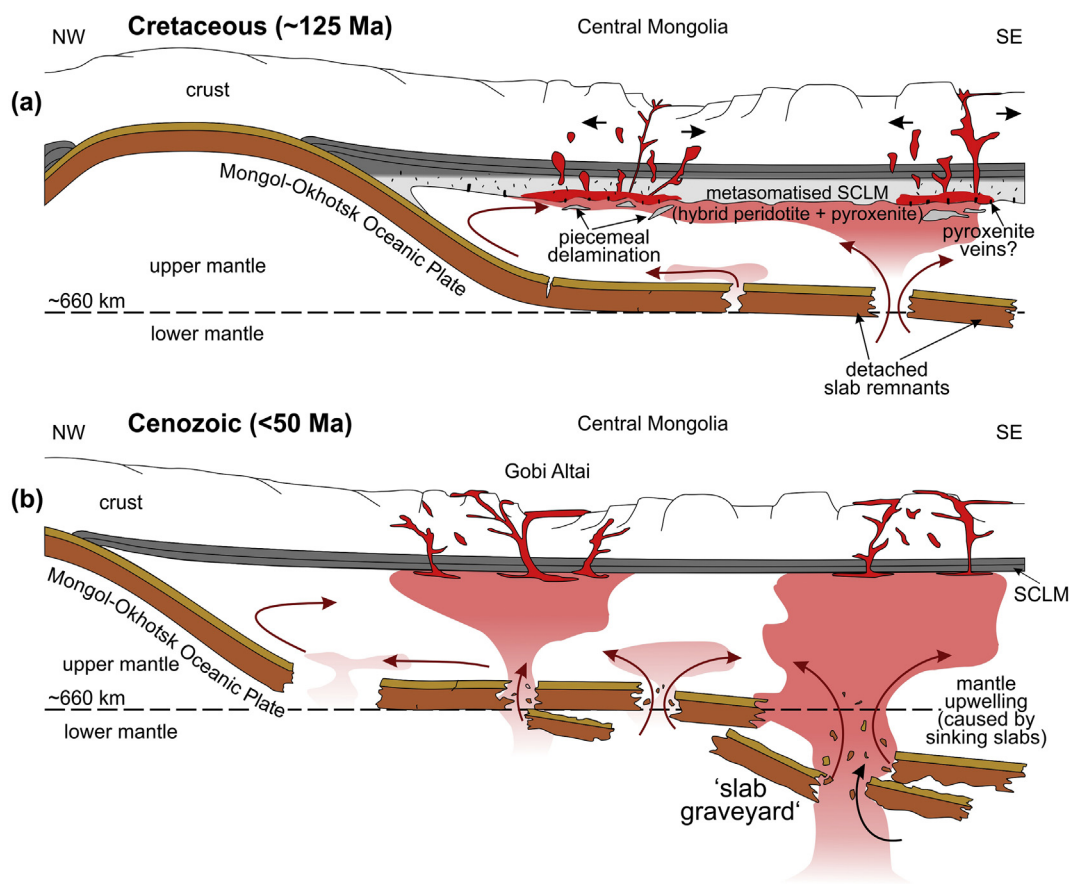


Fig. 14. Cartoon sketches of: a) Piecemeal delamination facilitated by previous compressional events associated with the double-sided subduction of the Mongol-Okhotsk Ocean. This closed ocean may have trapped asthenospheric mantle upwelling, controlling asthenospheric flow and assisting localized melting of a metasomatized subcontinental lithospheric mantle (SCLM). b) Slab graveyard under NE Asia associated with previous large-scale tectonic systems (closure of the Paleo-Asian and Mongol-Okhotsk oceans, and westerly subduction of the Paleo-Pacific plate) is foundering into the asthenospheric mantle and causing mantle upwelling.

Cenozoic volcanism across East Asia does not seem to have any obvious age distribution (e.g., Barry et al., 2003; Vorontsov et al., 2016; Liu et al., 2008; Wang et al., 2011; Yarmolyuk et al., 2015; Zhang and Guo, 2016), and limited Mg, Mo, and B isotope data for samples from NE China (Liu et al., 2019; Wang et al., 2017) indicates possible slab involvement. Although Pacific slab roll-back and convective erosion (above a big mantle wedge) processes likely facilitated Cenozoic magmatism in NE China, it is unclear to what extent Cenozoic magmatism in Mongolia was facilitated by this large-scale tectonic regime or from far-field effects of the India-Eurasia collision. The CAOB underwent a complex tectonic history associated with the closure of the Mongol-Okhotsk and Paleo-Asian oceans, and the westerly subduction of the Paleo-Pacific plate; these large-scale tectonic systems may have created a slab graveyard under East Asia (Van der Voo et al., 1999; Wei et al., 2012). We suggest that Cenozoic asthenospheric upwellings across East Asia was facilitated by slabs sinking into the upper mantle (Ancient Mongol-Okhotsk slabs and Pacific slabs) and contemporaneous tectonic processes associated with the Pacific Plate (Liu et al., 2019; Wu et al., 2019).

9. Conclusions

- (1) The Argalant Range Mesozoic magmatism has geochemical signatures consistent with the involvement of both peridotite and minor pyroxenite-like components. This pyroxenite-like component was obtained through the melting of metasomatized SCLM.
- (2) Mineral-liquid thermobarometer results for samples from Khukh Tolgoi and Samaan Damba indicate that upwelling

magma stalled at ~30 km depth before finally traversing further to surface.

- (3) The timing and spatial distribution of Early Cretaceous magmatic centers is not closely linked to styles of crustal deformation.
- (4) A model to explain Mesozoic magmatic genesis is presented here, whereby piecemeal delamination and convective erosion of a metasomatized SCLM drives magmatism.
- (5) The Mongolian Cenozoic volcanism also has geochemical signatures consistent with the melting of non-peridotite components. We suggest that magmatism from Togo contains the greatest amount of non-peridotite melt input, followed by Tariat and then Khangai Range Watershed localities.
- (6) A slab graveyard foundering into underlying mantle may be responsible for intermittent Cenozoic East Asian magmatism.

Declaration of Competing Interest

The authors declare that they have no known competing financial interests or personal relationships that could have appeared to influence the work reported in this paper.

Acknowledgements

M.N.D. acknowledges support from the Romanian Executive Agency for Higher Education, Research, Development and Innovation Funding project PN-III-P4-ID-PCCF-2016-0014.

The Petro Matad Group based in Ulaanbaatar, Mongolia provided field access, and administrative, logistical and financial support. We thank staff members Justin Tully, Bolor Erdenebat, and Davaa Buyan-Arivjikh for their assistance in all phases of the project.

Appendix A. Supplementary data

Supplementary data to this article can be found online at <https://doi.org/10.1016/j.lithos.2020.105747>.

References

- Badarch, G., Cunningham, W.D., Windley, B.F., 2002. A new terrane subdivision for Mongolia: implications for the Phanerozoic crustal growth of Central Asia. *J. Asian Earth Sci.* 21, 87–110.
- Barry, T.L., Saunders, A.D., Kempton, P.D., Windley, B.F., Pringle, M.S., Dorjnamjaa, D., Saandar, S., 2003. Petrogenesis of Cenozoic basalts from Mongolia: evidence for the role of asthenospheric versus metasomatized lithospheric mantle sources. *J. Petrol.* 44, 55–91.
- Barry, T.L., Ivanov, A.V., Rasskazov, S.V., Demonterova, E.I., Dunai, T.J., Davies, G.R., Harrison, D., 2007. Helium isotopes provide no evidence for deep mantle involvement in widespread Cenozoic volcanism across Central Asia. *Lithos* 95, 415–424.
- Burianek, D., Hanzl, P., Erban, V., Gilikova, H., Bolormaa, K., 2008. The early cretaceous volcanic activity in the western part of the Gobi-Altai rift (Shiliin Nuruu, SW Mongolia). *J. Geosci.* 53, 167–180.
- Burianek, D., Hanzl, P., Budil, P., Gerdes, A., 2012. Evolution of the early Permian volcanic-plutonic complex in the western part of the Permian Gobi-Altai Rift (Khar Argalant Mts., SW Mongolia). *J. Geosci.* 57, 105–126.
- Bussien, D., Gombojav, N., Winkler, W., Von Quadt, A., 2011. The Mongol–Okhotsk Belt in Mongolia—an appraisal of the geodynamic development by the study of sandstone provenance and detrital zircons. *Tectonophysics* 510, 132–150.
- Carlson, R.W., Ionov, D.A., 2019. Compositional characteristics of the MORB mantle and bulk silicate earth based on spinel peridotites from the Tariat Region, Mongolia. *Geochim. Cosmochim. Acta* 257, 206–223.
- Comeau, M.J., Becken, M., Käuffl, J.S., Grayver, A.V., Kuvshinov, A.V., Tserendug, S., Batmagnai, E., Demberel, S., 2020. Evidence for terrane boundaries and suture zones across Southern Mongolia detected with a 2-dimensional magnetotelluric transect. *Earth Planets Space* 72 (1).
- Cunningham, D., 2005. Active intracontinental transpressional mountain building in the Mongolian Altai: defining a new class of orogen. *Earth Planet. Sci. Lett.* 240, 436–444.
- Dash, B., Yin, A., Jiang, N., Tseveendorj, B., Han, B., 2015. Petrology, structural setting, timing, and geochemistry of cretaceous volcanic rocks in eastern Mongolia: Constraints on their tectonic origin. *Gondw. Res.* 27, 281–299.
- Davidson, J., Turner, S., Plank, T., 2012. Dy/Dy*: variations arising from mantle sources and petrogenetic processes. *J. Petrol.* 54, 525–537.
- Ducea, M.N., Seclaman, A.C., Murray, K.E., Jianu, D., Schoenbohm, L.M., 2013. Mantle-drip magmatism beneath the Altiplano-Puna plateau, Central Andes. *Geology* 41, 915–918.
- Enkhbold, A., Khukhuudei, U., Dorjgochoo, S., Ganbold, B., 2020. Morphology of Khorgo Volcano Crater in the Khangai Mountains in Central Mongolia. *Proc. Mongolian Acad. Sci.* 19–35.
- Gale, A., Dalton, C.A., Langmuir, C.H., Su, Y., Schilling, J.G., 2013. The mean composition of ocean ridge basalts. *Geochim. Geophys. Geosyst.* 14, 489–518.
- Gao, S., Rudnick, R.L., Yuan, H.L., Liu, X.M., Liu, Y.S., Xu, W.L., Ling, W.L., Ayers, J., Wang, X.C., Wang, Q.H., 2004. Recycling lower continental crust in the North China craton. *Nature* 432, 892–897.
- Gao, S., Rudnick, R.L., Xu, W.L., Yuan, H.L., Liu, Y.S., Walker, R.J., Puchtel, I.S., Liu, X., Huang, H., Wang, X.R., Yang, J., 2008. Recycling deep cratonic lithosphere and generation of intraplate magmatism in the North China Craton. *Earth Planet. Sci. Lett.* 270, 41–53.
- Gleeson, M.L., Gibson, S.A., Williams, H.M., 2020. Novel insights from Fe-isotopes into the lithological heterogeneity of Ocean Island Basalts and plume-influenced MORBs. *Earth Planet. Sci. Lett.* 535, 116114.
- He, L., 2014. Numerical modeling of convective erosion and peridotite-melt interaction in big mantle wedge: Implications for the destruction of the North China Craton. *J. Geophys. Res. Solid Earth* 119, 3662–3677.
- Herzberg, C., 2006. Petrology and thermal structure of the Hawaiian plume from Mauna Kea volcano. *Nature* 444, 605.
- Herzberg, C., Asimow, P.D., 2015. PRIMELT 3 MEGA. XLSM software for primary magma calculation: peridotite primary magma MgO contents from the liquidus to the solidus. *Geochim. Geophys. Geosyst.* 16 (2), 563–578.
- Herzberg, C., Cabral, R.A., Jackson, M.G., Vidito, C., Day, J.M.D., Hauri, E.H., 2014. Phantom Archean crust in Mangaia hotspot lavas and the meaning of heterogeneous mantle. *Earth Planet. Sci. Lett.* 396, 97–106.
- Hirschmann, M.M., 2000. Mantle solidus: Experimental constraints and the effects of peridotite composition. *Geochim. Geophys. Geosyst.* 1.
- Hofmann, A.W., White, W.M., 1982. Mantle plumes from ancient oceanic crust. *Earth Planet. Sci. Lett.* 57 (2), 421–436.
- Hunt, A.C., Parkinson, I.J., Harris, N.B.W., Barry, T.L., Rogers, N.W., Yondon, M., 2012. Cenozoic volcanism on the Hangai Dome, Central Mongolia: geochemical evidence for changing melt sources and implications for mechanisms of melting. *J. Petrol.* 53, 1913–1942.
- Johnson, C.L., 2015. Sedimentary basins in transition: distribution and tectonic settings of Mesozoic strata in Mongolia. *Geol. Soc. Am. Spec. Paper* 513, 513–517.
- Johnson, C.L., Greene, T.J., Zinniker, D.A., Moldowan, J.M., Hendrix, M.S., Carroll, A.R., 2003. Geochemical characteristics and correlation of oil and nonmarine source rocks from Mongolia. *AAPG Bull.* 87, 817–846.
- Johnson, C.L., Constenius, K.C., Graham, S.A., Mackey, G., Menotti, T., Payton, A., Tully, J., 2015. Subsurface evidence for late Mesozoic extension in western Mongolia: tectonic and petroleum systems implications. *Basin Res.* 27, 272–294.
- Käuffl, J.S., Grayver, A.V., Comeau, M.J., Kuvshinov, A.V., Becken, M., Kamm, J., Batmagnai, E., Demberel, S., 2020. Magnetotelluric multiscale 3-D inversion reveals crustal and upper mantle structure beneath the Hangai and Gobi-Altai region in Mongolia. *Geophys. J. Int.* 221 (2), 1002–1028.
- Kelemen, P.B., Hanghøj, K., Greene, A.R., 2003. One view of the geochemistry of subduction-related magmatic arcs, with an emphasis on primitive andesite and lower crust. *Treat. Geochem.* 3, 659.
- Kravchinsky, V.A., Cogné, J.P., Harbert, W.P., Kuzmin, M.I., 2002. Evolution of the Mongol–Okhotsk Ocean as constrained by new palaeomagnetic data from the Mongol–Okhotsk suture zone, Siberia. *Geophys. J. Int.* 148, 34–57.
- Lambart, S., Laporte, D., Schiano, P., 2009. An experimental study of pyroxenite partial melts at 1 and 1.5 GPa: Implications for the major-element composition of Mid-Ocean Ridge Basalts. *Earth Planet. Sci. Lett.* 288 (1–2), 335–347.
- Lambart, S., Baker, M.B., Stolper, E.M., 2016. The role of pyroxenite in basalt genesis: Melt-PX, a melting parameterization for mantle pyroxenites between 0.9 and 5 GPa. *J. Geophys. Res. Solid Earth* 121 (8), 5708–5735.
- Le Roux, V., Lee, C.T., Turner, S.J., 2010. Zn/Fe systematics in mafic and ultramafic systems: Implications for detecting major element heterogeneities in the Earth's mantle. *Geochim. Cosmochim. Acta* 74, 2779–2796.
- Lee, C.T.A., Luffi, P., Plank, T., Dalton, H., Leeman, W.P., 2009. Constraints on the depths and temperatures of basaltic magma generation on Earth and other terrestrial planets using new thermobarometers for mafic magmas. *Earth Planet. Sci. Lett.* 279, 20–33.
- Liu, J., Cai, R., Pearson, D.G., Scott, J.M., 2019. Thinning and destruction of the lithospheric mantle root beneath the North China Craton: a review. *Earth-Sci. Rev.* 196 paper 102873.
- Liu, Y., Gao, S., Kelemen, P.B., Xu, W., 2008. Recycled crust controls contrasting source compositions of Mesozoic and Cenozoic basalts in the North China Craton. *Geochim. Cosmochim. Acta* 72, 2349–2376.
- Ma, L., Jiang, S.Y., Hofmann, A.W., Xu, Y.G., Dai, B.Z., Hou, M.L., 2016. Rapid lithospheric thinning of the North China Craton: New evidence from cretaceous mafic dykes in the Jiaodong Peninsula. *Chem. Geol.* 432, 1–15.
- Meng, Q.R., 2003. What drove late Mesozoic extension of the northern China–Mongolia tract? *Tectonophysics* 369, 155–174.
- Menzies, M., Xu, Y., Zhang, H., Fan, W., 2007. Integration of geology, geophysics and geochemistry: a key to understanding the North China Craton. *Lithos* 96, 1–21.
- Nikolenko, A.M., Doroshkevich, A.G., Ponomarchuk, A.V., Redina, A.A., Prokopyev, I.R., Vladykin, N.V., Nikolaeva, I.V., 2020. Ar–Ar geochronology and petrogenesis of the Mughgai–Khudag alkaline-carbonatite complex (southern Mongolia). *Lithos* 372–373.
- Pang, C.J., Wang, X.C., Li, C.F., Wilde, S.A., Tian, L., 2019. Pyroxenite-derived Cenozoic basaltic magmatism in Central Inner Mongolia, eastern China: potential contributions from the subduction of the Palaeo-Pacific and Palaeo-Asian oceanic slabs in the Mantle transition Zone. *Lithos* 332, 39–54.
- Pearce, J.A., Norry, M.J., 1979. Petrogenetic implications of Ti, Zr, Y, and Nb variations in volcanic rocks. *Contrib. Mineral. Petrol.* 69, 33–47.
- Putirka, K.D., 2005. Igneous thermometers and barometers based on plagioclase + liquid equilibria: Tests of some existing models and new calibrations. *Am. Mineral.* 90, 336–346.
- Putirka, K.D., 2008. Thermometers and barometers for volcanic systems. *Rev. Mineral. Geochem.* 69, 61–120.
- Ripington, S., Cunningham, D., England, R., Hendriks, B., 2013. The crustal assembly of southern Mongolia: New structural, lithological and geochronological data from the Nemegt and Altan ranges. *Gondw. Res.* 23, 1535–1553.
- Sheldrick, T.C., Barry, T.L., Van Hinsbergen, D.J., Kempton, P.D., 2018. Constraining lithospheric removal and asthenospheric input to melts in Central Asia: a geochemical study of Triassic to cretaceous magmatic rocks in the Gobi-Altai (Mongolia). *Lithos* 296, 297–315.
- Sheldrick, T.C., Barry, T.L., Millar, I.L., Barfod, D.N., Halton, A.M., Smith, D.J., 2020a. Evidence for southward subduction of the Mongol–Okhotsk oceanic plate: implications from Mesozoic adakitic lavas from Mongolia. *Gondw. Res.* 79, 140–156.
- Sheldrick, T.C., Barry, T.L., Dash, B., Gan, C., Millar, I.L., Barfod, D.N., Halton, A.M., 2020b. Simultaneous and extensive removal of the East Asian lithospheric root. *Sci. Rep.* 10 (1), 1–6.
- Sobolev, A.V., Hofmann, A.W., Kuzmin, D.V., Yaxley, G.M., Arndt, N.T., Chung, S.L., Danyushevsky, L.V., Elliott, T., Frey, F.A., Garcia, M.O., Gurenko, A.A., 2007. The amount of recycled crust in sources of mantle-derived melts. *Science* 316, 412–417.
- Sorokin, A.A., Zaika, V.A., Kovach, V.P., Kotov, A.B., Xu, W., Yang, H., 2020. Timing of closure of the eastern Mongol–Okhotsk Ocean: Constraints from U–Pb and Hf isotopic data of detrital zircons from metasediments along the Dzhdzhdzhan Transect. *Gondw. Res.* 81, 58–78.
- Stolper, E., Asimow, P., 2007. Insights into mantle melting from graphical analysis of one-component systems. *Am. J. Sci.* 307 (8), 1051–1139.
- Sun, S.S., McDonough, W.F., 1989. Chemical and isotopic systematics of oceanic basalts: implications for mantle composition and processes. *Geol. Soc. Lond. Spec. Publ.* 42, 313–345.
- Thompson, R.N., Gibson, S.A., Dickin, A.P., Smith, P.M., 2001. Early cretaceous basalt and picrite dykes of the southern Etendeka region, NW Namibia: windows into the role of the Tristan mantle plume in Paranà–Etendeka magmatism. *J. Petrol.* 42, 2049–2081.

- Tomurtogoo, O., Windley, B.F., Kröner, A., Badarch, G., Liu, D.Y., 2005. Zircon age and occurrence of the Adaatsag ophiolite and Muroon shear zone, Central Mongolia: constraints on the evolution of the Mongol–Okhotsk Ocean, suture and orogen. *J. Geol. Soc. London* 162, 125–134.
- Van der Voo, R., Spakman, W., Bijwaard, H., 1999. Mesozoic subducted slabs under Siberia. *Nature* 397, 246.
- Van der Voo, R., van Hinsbergen, D.J., Domeier, M., Spakman, W., Torsvik, T.H., 2015. Latest Jurassic–earliest Cretaceous closure of the Mongol–Okhotsk Ocean: a palaeomagnetic and seismological-tomographic analysis. *Geol. Soc. Am. Spec. Paper* 513, 589–606.
- Van Hinsbergen, D.J., Cunningham, D., Straathof, G.B., Ganerød, M., Hendriks, B.W., Dijkstra, A.H., 2015. Triassic to Cenozoic multi-stage intra-plate deformation focused near the Bogd Fault system, Gobi–Altai, Mongolia. *Geosci. Front.* 6, 723–740.
- Villiger, S., Ulmer, P., Müntener, O., Thompson, A.B., 2004. The liquid line of descent of anhydrous, mantle-derived, tholeiitic liquids by fractional and equilibrium crystallization—an experimental study at 1·0 GPa. *J. Petrol.* 45, 2369–2388.
- Vorontsov, A.A., Yarmolyuk, V.V., Komaritsyna, T.Y., 2016. Late Mesozoic–early Cenozoic rifting magmatism in the Uda sector of Western Transbaikalia. *Russ. Geol. Geophys.* 57, 723–744.
- Wang, X.J., Chen, L.H., Hofmann, A.W., Mao, F.G., Liu, J.Q., Zhong, Y., Xie, L.W., Yang, Y.H., 2017. Mantle transition zone-derived EM1 component beneath NE China: Geochemical evidence from Cenozoic potassic basalts. *Earth Planet. Sci. Lett.* 465, 16–28.
- Wang, Y., Zhao, Z.F., Zheng, Y.F., Zhang, J.J., 2011. Geochemical constraints on the nature of mantle source for Cenozoic continental basalts in east-Central China. *Lithos* 125, 940–955.
- Wei, W., Xu, J., Zhao, D., Shi, Y., 2012. East Asia mantle tomography: New insight into plate subduction and intraplate volcanism. *J. Asian Earth Sci.* 60, 88–103.
- Windley, B.F., Alexeiev, D., Xiao, W., Kröner, A., Badarch, G., 2007. Tectonic models for accretion of the Central Asian Orogenic Belt. *J. Geol. Soc. London* 164, 31–47.
- Windley, B.F., Maruyama, S., Xiao, W.J., 2010. Delamination/thinning of sub-continental lithospheric mantle under Eastern China: the role of water and multiple subduction. *Am. J. Sci.* 310, 1250–1293.
- Wu, F.Y., Yang, J.H., Xu, Y.G., Wilde, S.A., Walker, R.J., 2019. Destruction of the North China craton in the Mesozoic. *Annu. Rev. Earth Planet. Sci.* 47, 173–195.
- Xiao, W., Windley, B.F., Sun, S., Li, J., Huang, B., Han, C., Yuan, C., Sun, M., Chen, H., 2015. A tale of amalgamation of three Permo–Triassic collage systems in Central Asia: oroclines, sutures, and terminal accretion. *Annu. Rev. Earth Planet. Sci.* 43, 477–507.
- Yang, Z.F., Zhou, J.H., 2013. Can we identify source lithology of basalt? *Sci. Rep.* 3, 1856.
- Yang, Z.F., Li, J., Jiang, Q.B., Xu, F., Guo, S.Y., Li, Y., Zhang, J., 2019. Using major element logratios to recognize compositional patterns of basalt: implications for source lithological and compositional heterogeneities. *J. Geophys. Res. Solid Earth* 124, 3458–3490.
- Yarmolyuk, V.V., Kudryashova, E.A., Kozlovsky, A.M., Lebedev, V.A., Savatenkov, V.M., 2015. Late Mesozoic–Cenozoic intraplate magmatism in Central Asia and its relation with mantle diapirism: evidence from the South Khangai volcanic region, Mongolia. *J. Asian Earth Sci.* 111, 604–623.
- Zhang, H.F., Sun, M., Zhou, X.H., Fan, W.M., Zhai, M.G., Yin, J.F., 2002. Mesozoic lithosphere destruction beneath the North China Craton: evidence from major-, trace-element and Sr–Nd–Pb isotope studies of Fangcheng basalts. *Contrib. Mineral. Petrol.* 144, 241–254.
- Zhang, M., Guo, Z., 2016. Origin of late Cenozoic Abaga–Dalinuoer basalts, eastern China: Implications for a mixed pyroxenite–peridotite source related with deep subduction of the Pacific slab. *Gondw. Res.* 37, 130–151.
- Zhang, Y., Yuan, C., Sun, M., Chen, M., Hong, L., Li, J., Long, X., Li, P., Lin, Z., 2019. Recycled oceanic crust in the form of pyroxenite contributing to the Cenozoic continental basalts in Central Asia: new perspectives from olivine chemistry and whole-rock B–Mo isotopes. *Contrib. Mineral. Petrol.* 174 (10), 83.